HHS Public Access

Author manuscript

*Cell Rep*. Author manuscript; available in PMC 2022 October 10.

Published in final edited form as:

*Cell Rep*. 2022 September 27; 40(13): 111412. doi:10.1016/j.celrep.2022.111412.

# A nuclear cAMP microdomain suppresses tumor growth by Hippo pathway inactivation

**Marek M. Drozdz**[1], **Ashley S. Doane**[2], **Rached Alkallas**[3,4,5], **Garrett Desman**[6], **Rohan Bareja**[2,7], **Michael Reilly**[1], **Jakyung Bang**[1], **Maftuna Yusupova**[1], **Jaewon You**[1], **Zuhal Eraslan**[1], **Jenny Z. Wang**[1], **Akanksha Verma**[2], **Kelsey Aguirre**[1], **Elsbeth Kane**[1], **Ian R. Watson**[3], **Olivier Elemento**[2,10], **Elena Piskounova**[1,10,12], **Taha Merghoub**[8,9,10,11,12], **Jonathan H. Zippin**[1,2,10,11,12,13,*]

[1]Department of Dermatology, Joan and Sanford I. Weill Medical College of Cornell University, New York, NY 10065, USA

[2]Englander Institute for Precision Medicine, Joan and Sanford I. Weill Medical College of Cornell University, New York NY 10065, USA

[3]Rosalind and Morris Goodman Cancer Institute, Department of Biochemistry, McGill University, Montreal, QC H3G 1Y6, Canada

[4]Department of Human Genetics, McGill University, Montréal, QC H3A 0C7, Canada

[5]McGill Genome Centre, McGill University, Montreal, QC H3A 0G1, Canada

[6]Department of Pathology and Laboratory Medicine, Icahn School of Medicine at Mount Sinai, New York, NY 10029, USA

[7]Institute for Computational Biomedicine, Joan and Sanford I. Weill Medical College of Cornell University, New York, NY 10065, USA

[8]Memorial Sloan Kettering Cancer Center, New York, NY 10065, USA

[9]Swim Across America and Ludwig Collaborative Laboratory, Immunology Program, Parker Institute for Cancer Immunotherapy at Memorial Sloan Kettering Cancer Center, New York, NY 10065, USA



[*]Correspondence: jhzippin@med.cornell.edu.

AUTHOR CONTRIBUTIONS

M.M.D., A.S.D., G.D., I.R.W., T.M., E.P., and J.H.Z. designed the experiments. M.M.D., A.S.D., G.D., R.B., M.R., J.B., M.Y., J.Y., Z.E., and R.A. generated the figures. M.M.D., J.Z.W., A.V., K.A., Z.E., and E.K. generated critical reagents or assisted with *in vivo* tumor experiments. M.M.D., O.E., T.M., E.P., I.R.W., and J.H.Z. wrote the manuscript with all authors providing feedback.

SUPPLEMENTAL INFORMATION

Supplemental information can be found online at https://doi.org/10.1016/j.celrep.2022.111412.

DECLARATION OF INTERESTS

J.H.Z. is a paid consultant and is on the medical advisory board of Hoth Therapeutics, is on the medical advisory board of SHADE, Inc., and is an inventor on US patent 8859213 on the use of antibodies directed against sACs for the diagnosis of melanocytic proliferations. O.E. is a cofounder and equity holder in Volastra Therapeutics and OneThree Biotech, an equity holder and SAB member in Owkin, Freenome, Genetic Intelligence, and Acuamark DX, and receives funding from Eli Lilly, Janssen, and Sanofi. T.M. is consultant for Leap Therapeutics, Immunos Therapeutics, and Pfizer, is a cofounder of Imvaq Therapeutics, has equity in Imvaq Therapeutics, reports grants from Bristol-Myers Squibb, Surface Oncology, Kyn Therapeutics, Infinity Pharmaceuticals, Peregrine Pharmeceuticals, Adaptive Biotechnologies, Leap Therapeutics, and Aprea, and is an inventor on patent applications related to work on oncolytic viral therapy, alphavirus-based vaccines, neo-antigen modeling, CD40, GITR, OX40, PD-1, and CTLA-4.

[10]Meyer Cancer Center, Weill Cornell Medicine, New York, NY 10029, USA

[11]Department of Pharmacology, Joan and Sanford I. Weill Medical College of Cornell University, New York, NY 10065, USA

[12]Senior author

[13]Lead contact

## SUMMARY

Cyclic AMP (cAMP) signaling is localized to multiple spatially distinct microdomains, but the role of cAMP microdomains in cancer cell biology is poorly understood. Here, we present a tunable genetic system that allows us to activate cAMP signaling in specific microdomains. We uncover a nuclear cAMP microdomain that activates a tumor-suppressive pathway in a broad range of cancers by inhibiting YAP, a key effector protein of the Hippo pathway, inside the nucleus. We show that nuclear cAMP induces a LATS-dependent pathway leading to phosphorylation of nuclear YAP solely at serine 397 and export of YAP from the nucleus with no change in YAP protein stability. Thus, nuclear cAMP inhibition of nuclear YAP is distinct from other known mechanisms of Hippo regulation. Pharmacologic targeting of specific cAMP microdomains remains an untapped therapeutic approach for cancer; thus, drugs directed at the nuclear cAMP microdomain may provide avenues for the treatment of cancer.

## Graphical Abstract

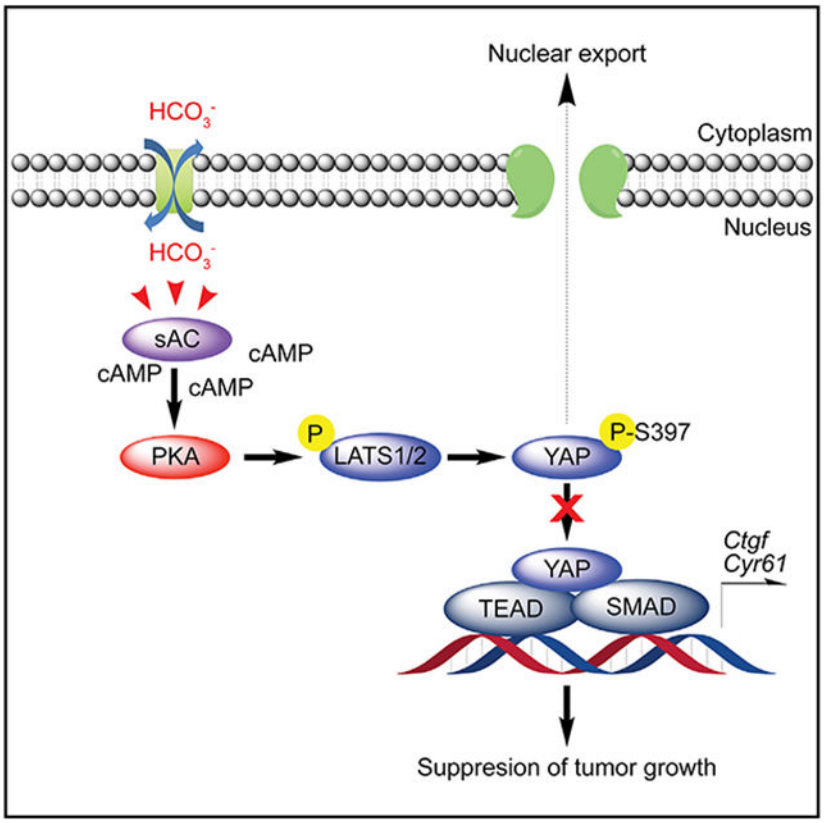

## In brief

Drozdz et al. develop a tunable genetic system allowing for the activation of cAMP sources in distinct organelles and subcellular domains. They discover that nuclear cAMP acts as a tumor suppressor in a wide range of human cancers through inactivation of the Hippo protein YAP inside the nucleus.

## INTRODUCTION

Cyclic AMP (cAMP), a ubiquitous second messenger, can induce a wide range of cellular responses including proliferation, differentiation, and migration in response to both extracellular (e.g., hormone) or intracellular (e.g., pH) signals (Chang and Oude-Elferink, 2014; Rehmann et al., 2007; Sassone-Corsi, 2012). cAMP is known to induce both tumor-promoting and tumor-suppressive effects in a variety of cancers (Baljinnyam et al., 2010; Coles et al., 2020; Johannessen et al., 2013; Kloster et al., 2008; Lyons et al., 2013; Michalides et al., 2004; Patra et al., 2018; Sheppard et al., 1984), also reviewed here (Fajardo et al., 2014). How these seemingly opposing roles of cAMP exist in cancer cells has remained unresolved. It has been proposed that these differential effects of cAMP in cancer could be explained by the existence of distinct microdomains of cAMP signaling, each having disparate effects on tumor cell biology (Beavo and Brunton, 2002; Desman et al., 2014; Musheshe et al., 2018; Torres-Quesada et al., 2017; Zaccolo, 2011).

In mammalian cells, two classes of adenylyl cyclases synthesize cAMP: transmembrane adenylyl cyclases (tmACs), which generate cAMP exclusively at the plasma membrane and endosomes, and the soluble adenylyl cyclase (sAC), which generates cAMP within both the cytoplasm and organelles, specifically the mitochondria and the nucleus (Cooper and Crossthwaite, 2006; Tresguerres et al., 2011). Adjacent to each source of cAMP are phosphodiesterases (PDEs), which prevent the diffusion of cAMP from one microdomain to another (Lohse et al., 2017; Musheshe et al., 2018). Multiple reports have shown that effector proteins of cAMP signaling (e.g., protein kinase A) can be spatially restricted even in cancer (Smith et al., 2017; Zhang et al., 2020a), suggesting that activation of different sources of cAMP in cancer cells may play an important regulatory role. However, the role of individual microdomain sources of cAMP, especially those that reside inside organelles, in tumor cell biology has remained poorly understood up to date.

The Hippo pathway plays an important regulatory role in cancer cell proliferation, invasion, and apoptosis (Yu et al., 2015). The Hippo signaling cascade is induced by a plethora of upstream chemical and physical stimuli and controls cancer cell proliferation and invasion, principally via the activity of YAP and TAZ (Zanconato et al., 2019), the two main transcriptional coactivators of the Hippo pathway. Even though the main site of YAP and TAZ function is inside the nucleus, how YAP or TAZ is regulated within the nucleus remains poorly described.

Here, we examined the effects of multiple distinct cAMP microdomains on cancer cell growth to address how this single second messenger can lead to such disparate effects in cancer. To address this fundamental question, we developed a tunable genetic system

that allows for the activation of spatially and temporally distinct cAMP microdomain signaling within a cell and in mice. We discovered the existence of a tumor-suppressive pathway evoked in multiple cancers solely by the sAC nuclear cAMP microdomain. We demonstrated that nuclear cAMP signaling induces the nuclear PKA-dependent, LATS-dependent phosphorylation of nuclear YAP solely at serine 397 (S397) without phosphorylation of YAP at S127 or phosphorylation of TAZ. Phosphorylation of nuclear YAP at S397 changed the rate of YAP export from the nucleus without affecting protein stability. Phosphorylation of S397 was required for nuclear cAMP-dependent YAP export from the nucleus and tumor growth suppression. Furthermore, nuclear cAMP signaling inhibited a pro-tumorigenic transcription program that highly correlated with low YAP-dependent gene expression across numerous human melanoma cell lines. Finally, our findings suggest that targeting the nuclear cAMP microdomain could be explored as a therapeutic approach for cancer treatment.

## RESULTS

### A nuclear cAMP microdomain is modulated in melanoma

The intraorganellar localization of sAC within mammalian cells is not static, and the presence of sAC in the nucleus is associated with early cellular transformation (Desman et al., 2014; Magro et al., 2012). It is well established that sAC is cytoplasmic in benign melanocytes (e.g., nevus), but upon transformation (e.g., melanoma *in situ*), nearly all melanocytes exhibit pan-nuclear sAC expression (Barnhill et al., 2013; Desman and Barnhill, 2016; Li et al., 2016; Magro et al., 2012; Solky and Zembowicz, 2014). Here, we determined whether sAC localization in the nucleus was stable upon tumor progression by measuring sAC localization in a panel of human melanoma biopsy samples (n = 34) (Table S1). sAC was frequently localized in the nucleus of melanoma cells that are present in the epidermis and reticular dermis (e.g., *in situ* and early invasive disease) (Figures 1A and 1B). In contrast, the nuclei of melanoma cells in invasive tumors of the deeper dermis tended to have nuclei lacking sAC protein (Figures 1C and 1D). We measured the tumor depth, using Breslow thickness, at which greater than 90% of melanoma cells have lost sAC protein in the nucleus (Abbas et al., 2014; Paek et al., 2007), and found that loss of sAC from the nucleus correlated significantly with melanoma depth ($p < 0.001$, likelihood-ratio test; Figures 1E and 1F). Thus, sAC was not stably localized in the nucleus during melanoma progression, and nuclear staining decreased significantly with the depth of tumor invasion (Figure 1G).

We previously reported that genetic deletion of all sAC-regulated microdomains sensitizes fibroblasts and keratinocytes to transformation (Ramos-Espiritu et al., 2016). We now show that transplantation of melanocytes with genetic inactivation of sAC (*Adcy10*$^{-/-}$, sAC$^{KO}$) leads to tumor formation in immunodeficient mice, while control wild-type (WT) immortalized melanocytes fail to grow in mice (Figures S1A-S1D). We reasoned that loss of sAC from a specific microdomain(s) might increase tumorigenic potential.

## Development of a genetic tunable system to investigate cAMP microdomains *in vitro* and *in vivo*

Because all sAC-defined microdomains are encoded by a single mRNA and protein, it is not feasible to genetically or pharmacologically activate or inhibit sAC in a single intracellular domain within a live cell or mouse with the currently available methods. Therefore, to assess the relative contribution of cAMP in different microdomains, we developed a genetic-based, tunable system allowing for the control of cAMP signaling in three spatially distinct microdomains not previously examined in cancer: nucleus (NLS-sAC), cytoplasm (NES-sAC), and mitochondria (mito-sAC) (Figure 2A). These microdomain-targeted constructs were introduced into a $sAC^{KO}$ mouse melanoma cell line to eliminate any contribution from endogenous sAC (Figure 2B). Doxycycline-induced expression of sAC in each microdomain was rapid (~1 h), dose dependent, and led to increased cAMP synthesis (Figures S1E-S1G). cAMP levels in a cell are tightly regulated and reflect a balance between adenylyl cyclase (AC)-dependent cAMP synthesis and cAMP degradation by PDEs within each microdomain (Cooper and Tabbasum, 2014; Lohse et al., 2017). Consistent with each of these targeted ACs forming PDE-regulated cAMP microdomains, inhibition of PDEs led to dramatic increases in cAMP compared with LacZ controls (Figure S1H). Mito-sAC-generated cAMP was previously shown to exclusively reside within the mitochondrial matrix, and cytoplasmic cAMP does not penetrate this microdomain (Acin-Perez et al., 2009a, 2009b; Valsecchi et al., 2017). Using an established, genetically encoded, live-imaging fluorescence resonance energy transfer (FRET)-based sensor of cAMP (Sample et al., 2012), we confirmed that NLS-sAC-dependent cAMP is localized only to the nucleus and that NES-sAC-dependent cAMP is localized only to the cytoplasm (Figure S1I). Therefore, microdomain-targeted ACs generate localized pools of cAMP and thus function biochemically similar to endogenous sACs (Acin-Perez et al., 2009b; Zippin et al., 2004). Our data demonstrate that we have generated a tunable genetic approach allowing us to test the role of cAMP in multiple intracellular domains. We next asked which microdomain(s) affected tumor cell proliferation.

## A nuclear cAMP microdomain suppresses tumor growth *in vitro* and *in vivo*

Mouse melanoma cell proliferation as three-dimensional colonies in Matrigel was unaffected by LacZ expression or an increase in cAMP signaling in the cytoplasm (NES-sAC) or inside the mitochondria (mito-sAC) (Figures 2C and 2D). In contrast, activation of nuclear cAMP signaling (NLS-sAC) inhibited the growth of melanoma cells in Matrigel (Figures 2C and 2D). We next established a panel of human and mouse cancer cell lines containing the doxycycline-inducible NLS-sAC cassette (Figure 2A) and found that activation of nuclear cAMP signaling reduced the growth of multiple human and mouse cancer cell lines *in vitro* (Figures 2E and S2). Next, we tested whether nuclear cAMP signaling affects tumor growth in mice. NSG mice were implanted with LacZ, NES-sAC, mito-sAC, or NLS-sAC melanoma cells, and, consistent with our observations in Matrigel, activation of cAMP signaling in the cytoplasm or mitochondria had no effect on tumor growth in mice; LacZ also had no effect (Figures 2F-2H and S3). In contrast, activation of nuclear cAMP signaling led to a significant inhibition of tumor growth as measured by a reduction in tumor diameter, tumor weight, and nuclear staining of a proliferation marker Ki67 (Figures 2F-2J and S3B). Our data show that sAC-dependent cAMP signaling in the nucleus, but not in mitochondria

or the cytoplasm, suppresses tumor cell proliferation, suggesting that cAMP has differential effects on proliferation depending on its localization.

## A nuclear cAMP microdomain alters chromatin accessibility and inhibits pro-tumorigenic gene expression profiles

We posited that nuclear cAMP signaling may suppress tumor cell growth by altering gene-expression profiles critical for tumor growth. RNA sequencing (RNA-seq) analysis of NES-sAC-, mito-sAC-, and NLS-sAC-expressing melanoma tumors revealed that cAMP in each microdomain led to significant changes in gene expression (Figure S4A). Whereas nuclear cAMP led to the most potent changes in gene expression, we observed that there was minimal overlap between the genes associated with each microdomain (Figures S4A and S5), further confirming limited cAMP diffusion (Acin-Perez et al., 2009b) between each sAC-defined microdomain. Gene set enrichment analysis (GSEA) revealed that nuclear cAMP led to specific changes in pathways predicted to suppress tumor growth, e.g., downregulation of Myc targets (Figures 3A and S4B). Furthermore, comparison of the most significant GSEA pathways upregulated or downregulated by nuclear cAMP (Figure S4B, left and right panels, respectively) to the other sAC-defined microdomains further confirmed that distinct cAMP microdomains evoke different gene-expression profiles in tumors.

To better understand the impact of nuclear cAMP on gene expression, we defined the chromatin accessibility regulatory landscape of NLS-sAC-expressing melanoma cells by assay for transposase-accessible chromatin sequencing (ATAC-seq). We constructed a chromatin accessibility atlas across cultured cells consisting of 66,275 ATAC-seq DNA elements and found that activation of nuclear cAMP signaling led to specific and significant changes in chromatin accessibility (Figures 3B, 3C, and S6). We identified 544 DNA elements with differential chromatin accessibility following NLS-sAC expression (false discovery rate [FDR] < 0.1; doxycycline [DOX] versus no DOX), compared with 97 DNA elements in LacZ-negative control experiments, suggesting changes in transcription factor (TF) activity upon nuclear cAMP activation. To address this point and considering that chromatin accessibility at TF DNA motifs reflects nucleosome displacement due to TF binding and chromatin remodeler recruitment (Shashikant and Ettensohn, 2019), we developed a computational method to infer the changes in TF accessibility re-modeling. We used this approach to study the relative contribution of 330 TFs expressed in these cells to the changes in chromatin accessibility (Figures 3D and S4C). Many of the TFs with decreased accessibility remodeling (e.g., TEAD, SMAD, RUNX) are important for tumorigenesis and are regulated downstream of signaling pathways with known roles in cancer (Grannas et al., 2015; Passaniti et al., 2017; Zhou et al., 2016), the Hippo pathway being among them (Yu et al., 2015). Thus, the Hippo pathway was predicted from our ATAC-seq data to be inhibited by nuclear cAMP.

RNA-seq performed in parallel to ATAC-seq (Figure S4D) revealed significant correlation between changes in chromatin accessibility of ATAC-seq DNA elements and the expression of genes adjacent to those elements (Figure S4E). GSEA of gene expression following NLS-sAC activation *in vitro* revealed significant enrichment in pathways that are relevant to tumor biology such as epithelial-to-mesenchymal transition and Myc signaling (Figure 3E).

We confirmed expression changes of several cancer-relevant genes identified by RNA-seq, including the reduced expression of the canonical Hippo pathway-dependent genes, e.g., *Ctgf* (also known as *Ccn2*) and *Cyr61* (also known as *Ccn1*) (Figures 3F and S4F) by qRT-PCR.

Interestingly, RNA-seq analysis from both tumors and cells showed that canonical cAMP-dependent melanocyte gene-expression profiles (e.g., Mitf) were unaffected by either cytoplasmic, mitochondrial, or nuclear sAC cAMP microdomains. We confirmed that, consistent with previous reports (Goding and Arnheiter, 2019; Hsiao and Fisher, 2014; Johannessen et al., 2013), activation of tmACs at the plasma membrane by G protein-coupled receptor (GPCR) agonists results in increased *Mitf* expression in melanoma cells, whereas induction of nuclear sAC does not (Figures S4G-S4I). These data taken together show that multiple cAMP microdomains defined by either sAC or tmACs regulate distinct gene-expression profiles in melanoma cells and suggest that NLS-sAC may regulate the Hippo signaling pathway.

## A nuclear cAMP microdomain induces YAP S397 phosphorylation via nuclear PKA and nuclear LATS activation

Our RNA-seq data suggested that NLS-sAC was inhibiting Hippo-dependent gene expression, and the canonical Hippo pathway can operate through either the YAP and/or TAZ transcriptional coactivators (Figure 4A) (Yu et al., 2015). In addition, cAMP signaling is reported to regulate YAP and TAZ activity; however, those studies were focused entirely on plasma-membrane-generated cAMP (Kim et al., 2013). Thus, we next asked whether nuclear cAMP signaling required YAP and/or TAZ activity. The LATS-dependent phosphorylation of specific serine residues is the principal mechanism of regulation for both YAP and TAZ (Zhao et al., 2010). Activation of nuclear sAC cAMP signaling increased LATS phosphorylation and, in turn, YAP phosphorylation at S397 (YAP-S397) but not at other YAP or TAZ serine residues (Figures 4B and S7A). NES-sAC and mito-sAC did not affect YAP or TAZ phosphorylation, suggesting that regulation of YAP-S397 is specific to the nuclear sAC cAMP signaling microdomain (Figures S7B-S7D). Consistent with published reports, GPCR-regulated cAMP led to the phosphorylation of YAP at multiple serine residues, as well as increased phosphorylation of TAZ at S89 (Figures S7E and S7F) (Yu et al., 2012). Thus, plasma membrane and nuclear cAMP microdomains, albeit differently, both regulate Hippo signaling by altering YAP phosphorylation, whereas cytoplasmic and mitochondrial cAMP microdomains have no effect on YAP or TAZ phosphorylation. We show in Figures 2E and S2 that nuclear cAMP inhibits the growth of several cancer cell lines; thus, we looked at their YAP-S397 phosphorylation status and found that S397 phosphorylation is induced by nuclear cAMP signaling across these cancer cells (Figure S7G).

Even though we do not observe any changes in TAZ phosphorylation following nuclear cAMP activation (Figures 4B and S7A), recent studies have suggested that sAC may affect TAZ activity, perhaps by changing TAZ expression (Wang et al., 2020). To firmly establish the necessity of YAP for nuclear sAC tumor suppression, we employed short hairpin RNAs (shRNAs) to knock down YAP or TAZ in melanoma cells (Figure S8A). Knockdown of

YAP prevented nuclear sAC inhibition of tumor cell growth in Matrigel (Figure 4C) and Hippo-dependent gene expression (Figure 4D), whereas knockdown of TAZ or expression of scrambled shRNA had no effect (Figures 4C and 4D).

Previous studies focused on cytoplasmic regulation of YAP report that YAP is phosphorylated at serine residues in a specific order, with S127 occurring before S397, and that phosphorylation at S127 may be required for S397 phosphorylation (Zhao et al., 2010). To determine whether S127 phosphorylation is required for nuclear cAMP regulation of S397 phosphorylation, we overexpressed S127A-YAP in melanoma cells. Nuclear cAMP signaling induced S397 phosphorylation of S127A-YAP protein; thus, S127 phosphorylation is not required for S397 phosphorylation in the nuclear cAMP microdomain (Figures 4E and S8B).

We performed cellular fractionation experiments on NLS-sAC melanoma cells, and, consistent with published reports (Li et al., 2014), we found that the LATS kinase localized within the nucleus (Figure 4F). Furthermore, activation of nuclear cAMP signaling induced the phosphorylation of the LATS kinase within the nucleus (Figure 4F). Thus, the nuclear cAMP signaling cascade leads to both nuclear LATS activation and nuclear YAP S397 phosphorylation. There are two LATS kinases expressed in mammalian cells, LATS1 and LATS2. We employed shRNA to test if nuclear cAMP-evoked signaling shows any bias towards LATS1 or LATS2 (Figure S8C). We observed that the knockdown of either LATS kinase significantly reduced S397 phosphorylation but did not abolish it completely (Figure S8D). This suggests that the nuclear cAMP domain may act through LATS1 and/or LATS2.

YAP-S397 phosphorylation by nuclear sAC was abolished by pharmacologic inhibition of sAC, thus cAMP generation within the nucleus is required (Figures 4G and S8E). LATS can be phosphorylated by the cAMP-effector protein PKA (Dasgupta and McCollum, 2019; Yu et al., 2013), and PKA holoenzyme is also present within the nucleus (Zippin et al., 2004); therefore, we tested whether PKA activity was required. Pharmacologic inhibition of PKA blocked NLS-sAC-induced YAP-S397 phosphorylation (Figures 4G and S8E). We also confirmed that LATS phosphorylation was blocked by inhibitors against sAC and PKA (Figure S8F). To confirm that the NLS-sAC-induced YAP S397 phosphorylation requires active LATS kinase, we incubated cells with the LATS1/2-specific inhibitor TRULI (Kastan et al., 2021). Incubation with TRULI led to complete suppression of NLS-sAC-induced YAP S397 phosphorylation (Figures 4G and S8E). These data confirm that NLS-sAC stimulates a nuclear cAMP microdomain leading to both PKA and LATS activation and YAP S397 phosphorylation.

### A nuclear cAMP microdomain increases the rate of YAP export from the nucleus

Phosphorylation of YAP can lead to its loss from the nucleus and/or its degradation (Dasgupta and McCollum, 2019; Zhao et al., 2007, 2010). We did not observe any change in YAP protein level following nuclear cAMP activation (Figures 4B and S7A). We next compared the effect of NLS-sAC activation and GPCR activation on YAP protein level in the presence of the protein translation inhibitor cycloheximide. Whereas NLS-sAC activation did not reduce YAP protein levels relative to control cells, GPCR-induced cAMP synthesis led to a reduction in total YAP levels (Figure S8G). Thus, we find no evidence to suggest

that nuclear cAMP reduces YAP protein stability, at least under the experimental conditions tested.

Since NLS-sAC activation did not affect YAP stability, we next asked if YAP localization within the nucleus was affected. Recent studies have demonstrated that YAP is constantly moving into and out of the nucleus and that the relative time spent within the nucleus is important for the regulation of YAP-dependent gene expression (Ege et al., 2018; Elosegui-Artola et al., 2017; Franklin et al., 2020; Manning et al., 2018; Shreberk-Shaked and Oren, 2019). We found that activation of nuclear cAMP signaling decreased YAP abundance in the nucleus (Figure 4H). This change in YAP subcellular distribution was blocked by pharmacologic inhibitors of sAC, PKA, and LATS (Figure 4H). To further confirm that nuclear PKA activity was required for the change in subcellular YAP localization by nuclear cAMP, we generated NLS-sAC melanoma cells that express NLS-PKI (Billiard et al., 2001) and found that NLS-PKI expression prevented the NLS-sAC-dependent change in YAP depletion from the nucleus (Figure 4I). The quantitation of nuclear and cytoplasmic YAP expression and total YAP detection across multiple conditions is summarized in Figure 4J. Since the movement of YAP into and out of the nucleus is a dynamic process, reduction of nuclear YAP levels suggested that the nuclear cAMP cascade either prevents YAP import and/or induces YAP export. To address this question, we generated NLS-sAC melanoma cells expressing EYFP-YAP (Ege et al., 2018) and performed fluorescence recovery after photobleaching (FRAP) analysis (Figure 4K). Consistent with published reports (Franklin et al., 2020; Manning et al., 2018; Shreberk-Shaked and Oren, 2019), we find that YAP moves into the nucleus under normal growth conditions within minutes (Figure 4L). Nuclear cAMP did not delay the immediate recovery after photobleaching but did prevent the recovery of YAP to WT levels (Figure 4L), suggesting that the import of YAP into the nucleus was not inhibited by nuclear sAC. Furthermore, inhibition of nuclear export with leptomycin B blocked the reduction of nuclear YAP levels following nuclear cAMP activation, suggesting that nuclear cAMP promotes YAP nuclear export (Figure 4L). Finally, we asked whether YAP S397 phosphorylation was required for the promotion of YAP export from the nucleus by nuclear cAMP. Overexpression of EYFP-YAP-S397A prevented nuclear cAMP from promoting the export of YAP from the nucleus (Figure 4M). Thus, our data suggest that nuclear sAC activation inhibits YAP by increasing the rate of nuclear export of YAP via phosphorylation of S397. We next examined whether YAP-S397 phosphorylation was necessary for nuclear cAMP-dependent suppression of tumor proliferation.

## YAP S397 phosphorylation is required for nuclear cAMP-induced tumor suppression

Using our NLS-sAC melanoma cell lines, we established subclones expressing either WT-YAP, S397A-YAP (S397A), S127A-YAP (S127A), or 5SA-YAP (5SA; five key regulatory S mutated to A, including S397) (Figures 4E and S9A) (Zhao et al., 2007, 2010). Nuclear cAMP signaling inhibited the proliferation of both WT-YAP- and S127A-overexpressing melanoma cells *in vitro* (Figure 5A); however, S397A and 5SA melanoma cells were insensitive to nuclear cAMP signaling, whether assessed by suppression of proliferation in Matrigel or mice (Figures 5A, 5B, S9B, and S9C). Of note, S397A and 5SA melanoma cells grew at a faster rate compared with WT-YAP melanoma cells *in vivo*. The NLS-sAC-induced reduction in the Ki67 proliferation marker (Figures 2I and

2J) was abolished by expression of S397A and 5SA YAP (Figures S9D and S9E). Thus, YAP-S397 phosphorylation is necessary for nuclear cAMP-dependent suppression of tumor proliferation.

## The endogenous sAC agonist bicarbonate induces YAP S397 phosphorylation in melanoma

Tumors grow in a relatively acidic microenvironment and are known to be metabolically active (Liberti and Locasale, 2016; Marino et al., 2012). This microenvironment is known to promote cancer growth and invasion (Liberti and Locasale, 2016; Marino et al., 2012). YAP is known to respond to products of metabolism, and Hippo signaling can affect multiple metabolic pathways (Koo and Guan, 2018; Zhang et al., 2018). sAC is a pH/metabolic sensor capable of responding to changes in the $CO_2$/bicarbonate/pH level in cells, which is in constant equilibrium (Chang and Oude-Elferink, 2014; Zippin et al., 2013). Thus, we reasoned that sAC may represent an additional link between pH and/or metabolism and Hippo signaling. Bicarbonate has been used as an agonist for endogenous sAC in mammalian cells (Zippin et al., 2004). To ensure bicarbonate stimulation of melanoma cells affects YAP 397 phosphorylation only through sAC, we first treated $sAC^{KO}$ melanoma cells with bicarbonate in the presence of a low dose of the PDE inhibitor IBMX. Under these conditions, bicarbonate did not affect YAP S397 phosphorylation (Figure 6A). In contrast, following nuclear sAC expression (DOX-induced NLS-sAC), bicarbonate did induce YAP S397 phosphorylation (Figure 6A). Bicarbonate stimulation, prior to DOX treatment, did not affect YAP S397 phosphorylation, similar to $sAC^{KO}$ melanoma cells, but enhanced YAP S397 phosphorylation following DOX treatment (Figure 6A). These data suggest that bicarbonate induces YAP S397 phosphorylation in a sAC-dependent manner. We next asked whether endogenously encoded sAC can lead to YAP S397 phosphorylation in response to bicarbonate. We first examined three human melanoma cell lines for sAC subcellular localization and found that sAC was expressed in the nucleus of all three cell lines (Figure 6B). We then stimulated each cell line with bicarbonate and observed a rapid phosphorylation of YAP at S397 (Figure 6C). Thus, bicarbonate can induce YAP S397 phosphorylation in melanoma cells via at least nuclear sAC (Figure 6D).

## Nuclear cAMP- and YAP-dependent signaling are inversely correlated in human melanoma

Recent reports suggest that changes in the YAP gene-expression profile may be the best measure of alterations in YAP activity (Franklin et al., 2020; Zhang et al., 2020b), and it has been shown that activation of YAP leads to a defined gene-expression pattern in human melanoma (Zhang et al., 2020b). We compared changes in RNA expression following overexpression of constitutively active 5SA-YAP mutant in the human melanoma cell line MeWo (Zhang et al., 2020b) with the changes in RNA expression induced by NLS-sAC in our mouse melanoma cells. NLS-sAC-dependent gene expression in mouse melanoma cells grown *in vitro* ($p = 1.08e{-}12$) or in mice ($p < 2e{-}16$) was inversely correlated with YAP-dependent gene expression in MeWo cells (Figure 7A). To validate this finding, we expanded our analysis to include 45 melanoma cell lines from the Cancer Cell Line Encyclopedia (CCLE) (see STAR Methods). We created three distinct gene sets for NLS-sAC and YAP, each enriched in genes that are strong indicators of NLS-sAC and YAP activities. Regardless of the gene set or enrichment approach used, NLS-sAC and

YAP activity signatures were anti-correlated across the melanoma cell lines (Figure 7B). In melanoma cell lines from the CCLE, YAP activity was shown to be associated with the differential expression of the marker genes identified by Hoek et al. (Hoek et al., 2006; Zhang et al., 2020b). To examine how NLS-sAC activity relates to YAP, we used consensus clustering to segregate melanoma cell lines from the CCLE into two groups based on the RNA expression of genes defined by Hoek et al. One group was characterized by higher NLS-sAC activity and lower YAP activity (motif 1). Conversely, the other group exhibited lower NLS-sAC activity and higher YAP activity (motif 2) (Figure 7C). Consistent with our model, these data suggest that NLS-sAC activation inhibits YAP signaling in human melanoma.

## DISCUSSION

For many years, it was unclear how a single second messenger could lead to such disparate effects in cancer. By taking a microdomain approach, we have uncovered a nuclear cAMP microdomain that functions as a tumor suppressor. The Hippo pathway is critical for numerous functions in cancer cells (Zanconato et al., 2019), and while cAMP is known to affect Hippo signaling, the specific sources of cAMP have remained largely undefined. Previous work has almost exclusively focused on understanding the regulation of YAP and TAZ in the cytoplasm; however, the main function of YAP and TAZ as transcriptional coactivators occurs in the nucleus. Interestingly, proteins that regulate YAP and TAZ, such as LATS, are known to be present in the nucleus, and nuclear LATS activation is reported (Li et al., 2014). We now reveal a role of nuclear cAMP as an inhibitor of nuclear YAP (Figure 6D). Regulation of YAP by the nuclear cAMP microdomain is distinct from GPCR-activated plasma membrane cAMP microdomains, which induce YAP phosphorylation on multiple serine residues (Figures S7E and S7F) and lead to YAP degradation (Figure S8G) (Kim et al., 2013; Yu et al., 2013). In contrast, nuclear cAMP signaling leads to nuclear LATS activation and phosphorylation of YAP solely at S397. Phosphorylation of YAP at S397 in the nucleus does not affect YAP protein stability but instead leads to nuclear export (Figures 4B, 4H-4M, S7A, and S8G). What mechanisms facilitate the nuclear cAMP-specific phosphorylation of YAP at S397 and its export from the nucleus remain important questions.

During this investigation, we have established that sAC defines at least three distinct cAMP microdomains capable of altering gene expression. Furthermore, we identify at least two distinct cAMP signaling cascades that regulate Hippo signaling: a GPCR-regulated tmAC cascade and a bicarbonate-regulated, nuclear sAC cascade. Thus, our data support the existence of multiple spatially distinct, differentially regulated cAMP microdomains defined by specific sources of cAMP leading to disparate effects in tumor cells. We anticipate that the investigation of individual cAMP microdomains will identify additional microdomain-specific cAMP signaling cascades in both tumor and benign cells.

It is well-established that cAMP signaling leads to specific changes in gene expression. However, we now reveal that multiple distinct cAMP-mediated pathways can lead to non-overlapping gene-expression changes in the same cell. For example, in melanocytes, the expression of the lineage-defining TF MITF and genes induced by MITF are used as

markers for cAMP-dependent gene expression (Goding and Arnheiter, 2019; Johannessen et al., 2013). We now reveal that MITF is only regulated by a subset of cAMP microdomains in melanocytes. Thus, MITF-dependent gene expression is not reflective of all cAMP signaling pathways in melanocytes. This fundamental appreciation of the complexities of cAMP-dependent gene expression are likely relevant for numerous cancer cell types and tissues.

It remains unknown what controls nuclear localization of sAC in cancer, and it will be important to establish which upstream signals affect the translocation of sAC into and out of the nucleus. We provide evidence for possible upstream signals important for the regulation of sAC when present in the nucleus. sAC is regulated by changes in cellular pH and metabolism (Chen et al., 2000; Zippin et al., 2001, 2013), which are known to influence tumor proliferation and metastasis (Spencer and Stanton, 2019; Zhu and Thompson, 2019). Intra- and extracellular pH and metabolism affect intracellular bicarbonate levels (Lee and Hong, 2020), and sAC activity is known to reflect changes in intracellular bicarbonate levels. We now show that changes in intracellular bicarbonate levels via sAC activity lead to YAP phosphorylation at S397 (Figure 6C). Whether additional metabolic- and/or pH-dependent signals regulate Hippo signaling via sAC is an open question.

Hippo signaling plays a critical role in the proliferation, differentiation, and apoptosis of nearly every cell and tissue type (Dasgupta and McCollum, 2019; Yu et al., 2015). Previous work has almost exclusively focused on the regulation of the Hippo signaling proteins YAP and TAZ in the cytoplasm. We have identified a previously unappreciated regulatory pathway of Hippo signaling that is distinct from established mechanisms. Nuclear cAMP-dependent regulation of Hippo signaling occurs in both mouse and human cells derived from a wide range of tissue types. Furthermore, we find that activation of nuclear cAMP signaling is strongly associated with the inactivation of YAP signaling in human melanoma (Figure 7). Therefore, nuclear cAMP-dependent regulation of Hippo signaling is likely to have broad-reaching and fundamental effects on a variety of cells, tissues, and organs.

## Limitations of the study

Most of the mechanistic experiments rely on the overexpression of sAC in the nucleus. The main reason for the use of overexpression is that all sAC microdomains are controlled by the same protein that is encoded by a single gene. Therefore, there is no genetic or pharmacologic method that can affect only nuclear sAC in live cells or mice. We do show that our nuclear sAC model is regulated in a similar manner to endogenous ACs. Furthermore, our nuclear sAC model leads to changes in gene expression that exhibit a highly significant inverse correlation with YAP-dependent gene expression across a large panel of 45 human melanoma cell lines. Therefore, while this model may have flaws, it is the best method available to study nuclear cAMP signaling in cells and mice and appears to be highly correlated to human disease.

We use the addition of extracellular bicarbonate to show that activation of endogenous sAC leads to phosphorylation of YAP at S397. Additional studies will be important to reveal which physiological sources of bicarbonate lead to sAC-dependent phosphorylation of YAP at S397.

Most of the mechanistic experiments in this study were performed in mouse melanoma cells; therefore, it will be important to expand the mechanistic studies of nuclear cAMP signaling in a variety of different cancer cells. In addition, it will be important to further resolve where within the nucleus sAC regulates YAP phosphorylation.

Our ATAC-seq data suggested that non-Hippo-dependent TFs had either increased or decreased binding to DNA; additional experiments are needed to determine the mechanisms affecting these TFs.

## STAR★METHODS

### RESOURCE AVAILABILITY

**Lead contact—**Further information and requests for resources and reagents should be directed to and will be fulfilled by the lead contact, Jonathan H. Zippin (jhzippin@med.cornell.edu).

**Materials availability—**All unique/stable reagents generated in this study (e.g. plasmids and cell lines) are available from the lead contact with a completed Materials Transfer Agreement.

#### Data and code availability

- Sequencing data from this study have been deposited at Gene Expression Omnibus and are publicly available as of the date of publication. Accession number: GEO: GSE154877. TOKEN: klwrqasazhgvbax. All other data reported in this manuscript will be shared by the lead contact upon request.
- This paper does not report original code.
- Any additional information required to reanalyze the data reported in this paper is available from the lead contact upon request.

### EXPERIMENTAL MODEL AND SUBJECT DETAILS

**Clinical data—**Post-diagnostic archival formalin-fixed paraffin-embedded tissue blocks and H&E slides from a total of 34 primary cutaneous malignant melanomas were retrieved from the IRB-approved melanoma database (IRB# 16-00816) within the Department of Pathology at the Mount Sinai Hospital. Sample collection was approved by the Program for the Protection of Human Subjects at the Icahn School of Medicine at Mount Sinai, and informed consent was obtained from all subjects. Case annotation of patient age, sex, tumor location, and AJCC pTNM stage were provided before histopathological examination (Table S1). Cases were evaluated by a board-certified dermatopathologist (GTD) for diagnostic confirmation of malignant melanoma, tumor subtype, Breslow thickness, Clark level, ulceration, and radial and vertical growth phases.

**Animal studies—**All procedures involving mice were performed with approval from the Weill Cornell Medical College Institutional Animal Care and Use Committee and were performed in compliance with institutional guidelines. Mice were maintained in ventilated

cages, on a standard rodent diet of chow or doxycycline diet (Global 2018 base with 625 mg/kg doxycycline hyclate; Teklad, #TD.01306) as indicated, and water ad libitum. Experiments were performed starting at 6-10 weeks of age on a sex-mixed cohort of in-house bred NSG mice.

**Cell lines used for *in vitro* experiments—**Generation of $Adcy10^{-/-}$ and $Adcy10^{WT/WT}$ melanocytes is described elsewhere (Zhou et al., 2018). Mouse melanoma Mel 2-4 line ($sAC^{KO}$) was derived from tumors formed by $Adcy10^{-/-}$ melanocytes injected subcutaneously into immunocompromised mice. Tumors were dissociated in trypsin immediately after removal from the mouse, placed in RPMI media supplemented with 2 mM glutamine, 50 U/mL of penicillin/streptomycin, and 10% heat-inactivated fetal bovine serum, and allowed to adhere to plastic tissue culture plates. Established Mel 2-4 melanoma line was characterized and authenticated by the Zippin Laboratory.

All SK-Mel lines and Yummer1.7 cells were provided by Taha Merghoub (Memorial Sloan Kettering Cancer Center, New York, NY), SCC12 was provided by Loraine Gudas (Weill Cornell Medical College, New York, NY), colon cancer lines (DLD1 and SW480) were provided by Lukas Edward Dow (Weill Cornell Medical College, New York, NY), pancreatic cancer lines (Hs766t, PANC1, MIAPaCa2) were provided by Lewis Cantley (Weill Cornell Medical College, New York, NY), prostate cancer cell line LNCaP was provided by Christopher Barbieri (Weill Cornell Medical College, New York, NY) and the melanoma M263 line was provided by Roger Lo (UCLA Medical Center). All cell lines were authenticated.

Mel 2-4, SK-Mel cell lines, M263 and prostate cancer cell lines were maintained in RPMI media, pancreatic and colon cancer cell lines were maintained in DMEM media while SCC12 and Yummer1.7 were maintained in DMEM/F12 medium. Each cell culture media was supplemented with 2 mM glutamine, 50 U/mL of penicillin/streptomycin, and 10% heat-inactivated fetal bovine serum. Additionally, for SCC12 cell line, the DMEM/F12 medium was supplemented with 400 ng/mL hydrocortisone, and for Yummer1.7 cells, the DMEM/F12 medium was supplemented with non-essential amino acids (Gibco, #11140-050).

All cells were maintained at 37°C in 5% $CO_2$.

**Bacterial strains—**DH10B Competent *E. coli* cells (ThermoFisher Scientific, #EC0113) were used for routine cloning and plasmid propagation. They were cultured in standard LB medium or plated on agar plates supplemented with appropriate antibiotic.

## METHOD DETAILS

**Immunohistochemistry on human melanoma biopsies—**Five micrometer thick unstained tissue sections containing tumor (N = 34) were created and stained under IRB approval (IRB# 16-00816) for R21 (anti-sAC, CEP Inc., 1:1000) using an automated Leica-Bond stainer platform. The percentage of tumor cells with nuclear sAC labeling within the epidermis and dermis were recorded. R21 nuclear expression was then evaluated at each Clark and AJCC-relevant Breslow thickness. Regions with 10% or greater nuclear staining

were considered positive and regions with less than 10% nuclear staining were considered negative.

***In vivo* tumor formation—**Tumor formation by wild type (sAC FF) and *Adcy10*$^{-/-}$ (sAC KO) melanocytes (n = 10 per cohort) was performed by injecting into both flanks 5,000,000 cells in 50 μL of 25% Matrigel Basement Membrane Matrix (Corning, #354248). Mice were observed every 3-4 days for tumor formation and tumor size was measured. Mice were euthanized when tumors reached 2 cm. For studies of the effects of cAMP microdomains on tumor growth, NSG mice were injected into the right flank with 5000 cells in 50 μL of 25% Matrigel Basement Membrane Matrix (Corning, #354248). Tumor growth was monitored every 3-4 days and the largest diameter was recorded. When tumors reached 1 cm in diameter, mice were randomized and one cohort was switched to doxycycline diet. When tumors in any cohort reached 2.5 cm in diameter, mice were euthanized, and tumor samples were collected for further analyses. Tumor growth data are presented as a fold change in size, normalized to tumor size on the day when mice were randomized and doxycycline was introduced into the diet. Upon euthanasia, tumors were removed, weighed, and samples were placed in formalin or flash frozen for subsequent analysis. Total number of mice per condition (regular chow/doxycycline chow): NLS-sAC 14/14, NES-sAC 9/9, mito-sAC 10/10, LacZ CTRL 5/5, 5SA-YAP 5/4, S397A-YAP 5/5, WT-YAP 5/5.

**Immunohistochemistry on tumor sections—**Tumor sections were fixed in 10% formalin solution (Sigma, #HT501128) and paraffin embedded. IHC was performed on the Leica Bond RX using the Bond Polymer Refine Detection Kit (#DS9800). The sections were pre-treated using heat mediated antigen retrieval with EDTA pH9 (Leica Biosystem Epitope Retrieval Solution 2, #AR9640) for 20 min. The sections were then incubated with R21 (Anti-sAC antibody, CEP Biotech, Inc, 1:1200) or Ki67 (CST, #12202, 1:500). Leica BOND red (R21) or diaminobenzidine (Ki67) was used as chromogen then counterstained with hematoxylin. Slides were imaged on an Olympus light microscope with 10× objective and DP71 camera. R21 staining was quantitated manually by GD and nuclear staining was compared to depth of tumor invasion (Breslow), clinical outcome, and the percentage and nuclear positive tumor cells was assessed. Quantification of Ki67 positive nuclei was performed with Fiji/ImageJ using raw data images. Color deconvolution H/DAB was applied, followed by RenyiEntropy threshold, and watershed tool to count the Ki67 positive nuclei per field (on average ~4,000 nuclei/image from doxycycline free condition were detected). 2-5 fields of non-necrotic sections were imaged per tumor, five tumors/condition (except NLS-sAC/regular chow, NES-sAC/doxycycline chow, and 5SA-YAP/doxycycline chow which were n = 4). Data in graphs are presented as a mean fold change over corresponding doxycycline-free condition ± SEM. For the purpose of figure preparation, contrast and brightness was adjusted by applying exactly the same settings to images from all the groups.

**Drug treatment—**Drugs were prepared according to manufacturers' instructions and added directly to cell culture medium. Doxycycline hyclate (Sigma, #D9891) was used as indicated. IBMX (3-Isobutyl-1-methylxanthine; Sigma, #I7018) was used at 10, 50 or 500 μM. PGE2 (Prostaglandin E2; Tocris, #2296) was used at 10 μM. Isoproterenol

hydrochloride (Calbiochem, #420355) was used at 10 μM. LRE1 (Sigma, SML1857) was used at 50 μM. KT5720 (Sigma, #K3761) was used at 10 μM. TRULI (gift from the Tri-I TDI) was used at 500 nM. Leptomycin B (Cayman Chemical Company, # 10004976) was used at 46 nM. Cycloheximide (Sigma, # 01810) was used at 20 μg/mL.

Bicarbonate stimulation of human melanoma cells was performed under ambient $CO_2$ conditions at 37°C. Cells were cultured in pH 7.2 stabilized media deficient in bicarbonate for 6 h, and then stimulated by replacing media with regular culture media containing bicarbonate.

**Plasmid DNA, primers, and cloning—**The following plasmids were obtained from Addgene: pCW57.1 (Addgene plasmid, #41393); pcDNA3-ICUE3 (Addgene plasmid, # 61622) (DiPilato and Zhang, 2009). GFP-PKI nls (Addgene plasmid, #118301) (Billiard et al., 2001); pLL3.7-EF-EYFP-YAP1_WT-PolyA (Addgene plasmid, #112284) (Ege et al., 2018); pQCXIH-Myc-YAP (Addgene plasmid, #33091) (Zhao et al., 2007); pQCXIH-Myc-YAP-5SA (Addgene plasmid, #33093) (Zhao et al., 2007); pQCXIH-Flag-YAP-S127A (Addgene pasmid, # 33092) (Zhao et al., 2007); and pQCXIH-Flag-YAP-S381A (Addgene plasmid, #33068) (Zhao et al., 2010). Of note, YAP S381 in mice corresponds to residue S397 in humans; all reference to phosphorylation at this site was described as S397.

**EYFP-YAP-S397A plasmid was created from pLL3.7-EF-EYFP-YAP1_WT-PolyA by site-directed mutagenesis and confirmed by sequencing—**sACt (Buck et al., 1999) was tagged with either two NLS or NES sequences (Dang and Lee, 1988; Fu et al., 2013; Wen et al., 1995). List of primers used for cloning is provided in Table S2. Mito-sAC (Acin-Perez et al., 2009a) was provided by Giovanni Manfredi (Weill Cornell Medical College, New York, NY). Gateway cloning system (Thermo) was used to clone sAC into the pCW57.1 plasmid. LacZ was shuttled into pCW57.1 from the pLenti6.3_V5-GW_lacZ plasmid.

**Gene knockdown—**LATS1 and 2 knock-down was achieved using GIPZ lentivirus specific for mouse LATS1 or 2 mRNA (Dharmacon #RMM4532-E-EG50523, and #RMM4532-EG16798).

Knock-down of YAP or TAZ was achieved by lentiviral delivery of shRNA encoded by pRRL.SFFV.GFP.mirE.PGK.Neo.Yap1.891 and pRRL.SFFV.GFP.mirE.PGK.Neo.Wwtr1.1533 respectively (a kind gift from Dr. Lukas Edward Dow). A lentiviral-based non-targeting shRNA control was purchased from Origene (Origene #TR30021V).

Transduced cells were selected based on GFP expression (selection marker encoded by the lentivirus delivered DNA), and single clones for YAP, TAZ, or LATS1/2 shRNA knock-down were established for downstream experiments.

**Intracellular cAMP ELISA—**Cells were seeded in 24-well plate at $2 \times 10^5$ cells per well. Doxycycline was added at 1 μg/mL for the time indicated. 500 μM 3-Isobutyl-1-methylxanthine (IBMX, Sigma, #I7018) was supplemented to the media for the indicated

time. Adherent cells were lysed directly in 200 μL of 0.1 M HCl, and the intracellular cAMP content was determined using the cAMP complete ELISA kit (ENZO Life Sciences, # ADI-901-066). Data is represented either as a fold change in cAMP level over untreated cells, or pg/mL cAMP accumulated per $10^5$ cells.

**Lentivirus generation and clone selection—**293T cells were transfected with pMD2.G enveloping plasmid, psPAX.2 packaging plasmid, and either plasmids encoding microdomain-targeted sAC (pCW57.1 constructs), or YAP variants (pQCXIH constructs). Medium containing viral particles was collected approximately 60 h later, passed through a 0.45 μm filter and used immediately. For infection, lentivirus was added with polybrene (Sigma, #H9268) at 6 μg/mL. The next day cell culture medium was replaced, and drug selection was started 24 h later. Puromycin dihydrochloride (Sigma, #P8833) was used to select sAC expressing cells at 1-7.5 μg/mL depending on the cell line. Hygromycin B (Sigma, #H3274) was used at 200 μg/mL to select cells expressing YAP variants.

**Immunocytochemistry and fluorescent light microscopy—**Cells were seeded on glass coverslips and grown as a monolayer. They were fixed with 4% paraformaldehyde (Electron Microscopy Sciences, #15710) for 10 min, permeabilized in 0.5% Triton X-100 (Sigma, #X100) in PBS for 5 min, and blocked in 3% bovine serum albumin (Proliant Biologicals, #68100) for one hour. Immunolabeling with primary and secondary antibodies was conducted for one hour at room temperature. Primary antibodies targeted: HA-Tag (C29F4; CST, #3724; dilution 1:500), sAC (R21; CEP Inc.; dilution 1:100), YAP (D8H1X; CST, #14074; dilution 1:100), and cytochrome C (2CYTC-199; Santa Cruz, #sc-81752; dilution 1:50). Secondary antibodies used were donkey anti-mouse and donkey anti-rabbit conjugated to Alexa Fluor 488 or Alexa Fluor 647 (Thermo, #A-21206, #A-31571, #A-31573) and diluted 1:300. Coverslips were mounted on glass microscopy slides with ProLong Gold Antifade Mountant with DAPI (Thermo, #P36931). Immunostained cells were imaged on a Zeiss LSM 880 Inverted laser scanning microscope (Zeiss, Oberkochen, Germany) using a Plan-Apochromat 40x/1.3 Oil DIC M27 immersion lens. Images were acquired using ZenBlack operating software. Any quantitation performed, was done using raw data images. For the purpose of figure preparation, contrast and brightness was adjusted by applying exactly the same settings to images from control and experimental groups.

**YAP nuclear localization analysis—**Microscopy images were acquired as described above. Quantitative analyses were performed using ImageJ 2.0 (Wayne Rasband, NIH, USA). Nuclei were identified by DAPI stain. To define regions of interest, the YAP microscopy image threshold was set to pixel intensity greater than 10 and converted to binary image. Erosion, followed by dilation operation, was performed to remove isolated pixels. Such regions of interest were applied to raw YAP microscopy images and the total pixel intensity, corresponding to the total YAP signal was calculated per cell. The nuclear region was defined by DAPI stain, and used to calculate the nuclear YAP signal on a per cell basis. Cytoplasmic YAP signal was determined by subtracting nuclear YAP signal from the total YAP signal. Nuclear to cytoplasmic ration (N/C) was calculated per cell. To study effects of PKI on YAP cellular localization, cells were transfected with NLS-PKI-GFP expressing plasmid (Addgene, #118301), and used for experiments 24 h later. NLS-PKI

expressing cells were identified by GFP fluorescence. Data was normalized to untreated control cells and presented as mean with SEM. Each experimental condition was repeated 3-5 times.

**YAP nuclear export analysis—**Fluorescent recovery after photobleaching (FRAP) was performed on a Zeiss LSM 880 Inverted laser scanning microscope (Zeiss, Oberkochen, Germany) fitted with temperature-controlled and $CO_2$ chamber for live cell work using a Plan-Apochromat 40x/1.3 Oil DIC M27 immersion lens. Images were acquired using ZenBlack operating software. EYFP-YAP expressing cells were seeded in 35 mm glass bottom dishes (MatTek). After 24 h incubation with or without doxycycline, nuclear region was bleached with 405 nm laser wavelength, to reduce nuclear EYFP-YAP signal by at least 70%. Recovery of EYFP-YAP signal inside the nucleus was measured every 5 s over indicated time. Mean fluorescent intensity data was normalized by setting the initial fluorescence signal (pre-bleach) to 100%, and the signal immediately after photo-bleaching (timepoint 0) to 0%. Normalized recovery of EYFP-YAP signal inside the nucleus is presented from timepoint 0s. EYFP-YAP fluorescence in adjacent, non-bleached nuclei remained constant.

**Intracellular cAMP measurement in live cells—**Cells were transfected with the cAMP FRET probe ICUE3 (DiPilato and Zhang, 2009; Sample et al., 2012). Briefly, cells were seeded in a 24-well μ-Plate (iBiDi, #82406) and grown overnight either with or without 1 μg/mL doxycycline. Next day, cells were washed twice and maintained in Hank's balanced salt solution in a $CO_2$-independent incubator. After 10 min equilibration time, they were treated with 15 mM $NaHCO_3$. Images were acquired on a Zeiss LSM 880 Inverted laser scanning microscope (Zeiss, Oberkochen, Germany) fitted with temperature-controlled chamber for live cell work using a Plan-Apochromat 40x/1.3 Oil DIC M27 immersion lens. Images were acquired every 30 s using ZenBlack operating software. Dual emission ratios were obtained with 405 nm wavelength excitation, and emission filters cycled between 475/40 nm for cyan fluorescent protein and 535/25 nm for yellow fluorescent protein present in ICUE3. Images were analyzed in ImageJ 2.0 (Wayne Rasband, NIH, USA). Background correction was performed by subtracting autofluorescence of regions without cells from the emission of cells expressing ICUE3. Intensity of cyan and yellow fluorescent protein was measured in both cytoplasmic and nuclear regions within each cell and cyan to yellow ratio was calculated. The ratio change over the bicarbonate stimulation was then normalized to the ratio of image acquired immediately after adding bicarbonate (set to 1).

**Immunoblotting—**Primary antibodies used for Western Blot analysis: HA-Tag (C29F4; CST, #3724), YAP (D8H1X; CST, #14074), Phospho-Ser397 YAP (D1E7Y; CST, #13619), Phospho-Ser127 YAP (D9W2I; CST, #13008), Phospho-Ser109 YAP (CST, #46931), Lats1 (C66B5; CST, #3477), Lats1 (CST, #9153), Phospho-Thr1079 Lats1 (D57D3; CST, #8654), Phospho-Ser909 Lats1 (CST, #9157), TAZ (D3I6D; CST, #70148), Phospho-Ser89 TAZ (E1X9C; CST, #59971), GAPDH (14C10, CST, #2118), H3 (Abcam, #ab1791), and Beta-tubulin (TUB2.1, Sigma, #T4026). All antibodies were used at the manufacturer's suggested dilutions. Secondary antibodies: HRP linked anti-rabbit IgG (CST, 7074), and HRP linked anti-mouse IgG (Amersham, #NXA931) were used at the manufacturer's

recommended dilutions. Cultured cells were lysed directly in SDS-PAGE sample loading buffer (50 mM Tris-Cl, pH 6.8; 2% SDS, 6% (v/v) glycerol; 0.01% (w/v) bromophenol blue) containing 5% 2-mercaptoethanol, heated at 95°C for 5 min, electrophoresed in 8 or 10% Tris gels, and transferred to nitrocellulose membranes (GE Life Sciences, #10600002). The membranes were blocked in TBST (Tris-buffered saline, 0.1% Tween 20) containing 5% Bovine Serum Albumin. Antibodies were diluted in blocking buffer. Incubation with primary antibodies was performed at 4°C overnight, while incubation with HRP-conjugated secondary antibodies was performed at room temperature for one hour. Protein bands were detected with SuperSignal West Femto enhanced chemiluminescence substrate (Thermo, #34096) or HyGlo Quick Spray (Denville, #E2410). When necessary, the membranes were reprobed after incubation in Restore Western Blot stripping buffer (Thermo, #21059). GAPDH or Beta-tubulin antibodies were used as loading controls. Tumor samples were homogenized in RIPA buffer (Thermo, #89901) followed by protein concentration measurement using DC Protein Assay (Bio-Rad, #5000112). Tumor lysates were immunoblotted as above. Membranes were stripped with Western Blot Strip-It Buffer (Advansta, # R-03722-D50). Quantitation of Western blot band volumes was performed in Image Lab 6.1 (Bio-Rad Laboratories) using non-saturated raw data images. For the purpose of figure preparation, black color balance was adjusted to 10% across all the Western images shown in the paper.

**Nuclear fractionation—**Fractionation of intact nuclei from cytoplasm was performed using Nuclei Isolation Kit: Nuclei EZ Prep (Sigma, #NUC101-1KT) following manufacturer's instructions. For Western blot analysis equal cell equivalents were loaded for nuclear and cytoplasmic fractions.

### *In vitro* cancer cell growth

**Matrigel assay:** *In vitro* cancer cell growth in 3D matrix was performed as previously described (Pauli et al., 2017) with modifications. 96-well plates with white walls and clear bottom (Corning, #3610) were coated with 40 μL of 3 mg/mL Matrigel matrix solution (Corning, #356231). Cell suspension was mixed with Matrigel (1:2) and 1000 cells were seeded per well. Wells were topped with culture media with or without doxycycline and kept in a cell incubator (37°C, 5% $CO_2$) for 7-14 days until organoids formed. Media was replenished every 2-3 days. Viability of tumor organoids was assessed by CellTiter-Glo® 2.0 assay (Promega, #G9242) according to manufacturer's instructions. Luminescence was measured using a SpectraMax plate reader. Of note, since adenylyl cyclases consume ATP to generate cAMP, we confirmed that overexpression of each microdomain targeted cyclase had no effect on cellular ATP levels; thus, ATP measurements were reflective of cell number and not cyclase activity.

**Clonogenic assay:** 3000-5000 cells/well were seeded in 6 well plates and incubated at 37°C in $CO_2$ incubator. The next day doxycycline was added to wells. Media was changed every 2-3 days. After 11-14 days, the plates were washed with phosphate buffered saline (PBS), fixed with 10% formalin for 40 min, stained with 0.01% crystal violet diluted with $dH_2O$ for 1 h, rinsed with $dH_2O$, and allowed to air dry overnight. Colony formation was assessed by photography and by dissolving the crystal violet-stained cells with 10% acetic

acid (Spectrum Chemical, #AC110) solution diluted in $dH_2O$ for 30 min. Crystal violet absorbance was measured at 590 nm using a SpectraMax plate reader.

## Genomic data analysis

**RNA-seq:** Total RNA was isolated using the RNeasy mini kit (Qiagen, # 74104). Following RNA isolation, total RNA integrity was checked using a 2100 Bioanalyzer (Agilent Technologies, Santa Clara, CA). RNA concentrations were measured using the NanoDrop system (Thermo Fisher Scientific, Inc., Waltham, MA). Preparation of RNA sample library and RNA-seq were performed by the Genomics Core Laboratory at Weill Cornell Medicine. Messenger RNA was prepared using TruSeq Stranded mRNA Sample Library Preparation kit (Illumina, San Diego, CA, # 20020595), according to the manufacturer's instructions. The normalized cDNA libraries were pooled and sequenced on Illumina HiSeq4000 sequencer with pair-end 50 cycles.

Transcript abundances were quantified using Salmon version 1.2.0 (Patro et al., 2017) by selective alignment with a decoy-aware transcriptome index of Gencode Release M23 (GRCm38.p6, https://www.gencodegenes.org/mouse/release_M23.html). Transcript abundance estimates from Salmon were imported into R and summarized to annotated gene counts using the BioConductor package TXImeta (Love et al., 2020). Differential expression was computed using the BioConductor package DESeq2 (Love et al., 2014). Gene set enrichment analysis (GSEA) was performed using the genome-wide $Log_2$ fold-changes for each microdomain. Gene sets with positive enrichment were reported as up-regulated, and those with negative enrichment were reported as down-regulated, and significance was determined using a 1% FDR.

Number of tumor samples used for RNA-seq analysis was n = 2 per cell type (NLS-sAC, NES-sAC, mito-sAC) per condition (regular chow vs doxycycline chow) for a total of n = 12. We used a software package called Deseq2 (Love et al., 2014) to calculate statistical significance for differences in gene expression from a small number of samples (n = 2 per group). This method uses a generalized linear model to "borrow" information about the variance in a gene's expression from other genes with similar average expression, increasing statistical power to detect changes in expression from small numbers of samples. RNA-seq on cells treated *in vitro* was performed on three NLS-sAC clones, with (48 h) or without doxycycline, in parallel with two LacZ control lines, with (48 h) or without doxycycline, for a total of n = 10.

**ATAC-seq:** ATAC-seq library preparation and sequencing was performed at the Epigenomics Core at Weill Cornell Medicine by using the OMNI-ATAC-seq method described by Corces (Corces et al., 2017). Briefly, 50,000 cells at ~70% viability were spun down and incubated 3 min at 4°C in 25μL of a detergent buffer containing 0.2% Igepal CA-630 (Sigma, #I8896), 0.2% Tween 20 (Sigma, #P9416) and 0.02% Digitonin (Promega Corporation, #G9441). Nuclei were centrifuged at 500 g for 10 min and immediately resuspended in 25 μL of buffer containing 2.5 μL of Tn5 transposase (Illumina, #15027865) for a 30 min incubation at 37°C. Fragments generated by the Tn5 transposase were purified using the DNA Clean and Concentrate kit (Zymo Research, #D4014). Uniquely indexed

libraries were obtained by amplification of the purified fragments with indexed primers using 10 cycles of PCR (5 min × 72°C, 5 cycles each 10 s × 98°C, 30 s × 63°C, 1 min × 72°C). Resulting libraries were subjected to a two-sided size clean up using SPRI beads (Beckman Coulter, Brea, CA) to obtain sizes between 200 and 1000 bp, and pooled for sequencing. The pool was clustered at 9 pM on a pair end read flow cell and sequenced for 50 cycles on an Illumina HiSeq 2500 to obtain ~40M reads per sample. Primary processing of sequencing images was done using Illumina's Real Time Analysis software (RTA) as suggested by the Illumina. CASAVA 2.17 software was used to perform image capture, base calling and demultiplexing of the raw reads. Paired-end 50 base pair ATAC-seq reads were trimmed to remove adapter sequences using NGmerge with options "-u 41 -a" (Gaspar, 2018). Trimmed read pairs were aligned to version 38 of the mouse reference genome (GRCm38) using bowtie2 with the following options: "-X2000 –local –mm -k 4". Aligned reads were filtered and sorted to exclude reads mapping to mitochondrial DNA and black-listed regions, and duplicate read pairs were removed using the "MarkDuplicates" program in picard tools (http://broadinstitute.github.io/picard), resulting in a final aligned, sorted, and filtered BAM file that was used for all subsequent analysis.

ATAC-seq peaks were called from Tn-5 corrected insertions using MACS2 callpeak with option "-g hs –nomodel –shift −75 –ext-size 150 –keep-dup all –call-summits". A chromatin accessibility atlas containing 500 bp disjoint genomic intervals (DNA elements) was constructed from called peak summits across all primary cells using an iterative peak-ranking method as previously described (Corces et al., 2018). To quantify accessibility across samples, the number of single-base Tn5-corrected insertions that fell within each 500 bp DNA element was counted from ATAC-seq bam files using the command "pyatac counts" in the nucleoATAC package (Schep et al., 2015). Differential accessibility between conditions was computed using DESeq2. Normalization factors included in the call to DESeq2 were computed by quantile normalization with GC sequence content bias correction using the EDAseq BioConductor package. Chromatin accessibility $Log_2$ fold-changes were computed and shrunken using the function "lfcShrink" with option "type = ape" in the DESeq2 R package (Zhu et al., 2019). Differentially accessible DNA elements were identified at FDR of 10%. All gene-based annotation was performed using Gencode Release M23 (GRCm38.p6, https://www.gencodegenes.org/mouse/release_M23.html). DNA elements were assigned to genes according to the nearest TSS of a protein coding gene.

Annotated transcription factor motifs were identified in genomic DNA spanning the 500 bp DNA elements using the R package motifMatchR version 1.8.0 (https://bioconductor.org/packages/release/bioc/html/motifmatchr.html) with the options "p.cutoff = 1e-6". A filtered and curated collection of mouse transcription factor motifs was obtained from chromVARmotifs ("mouse_pwms_v2", https://github.com/GreenleafLab/chromVARmotifs) (Schep et al., 2017). Transcription factor motifs were filtered to include those in which the corresponding transcription factor was expressed with transcript abundance >1 TPM in at least one replicate experiment (see RNA-seq methods). To calculate change in accessibility remodeling, we performed a linear regression of the shrunken $Log_2$ fold-changes on each TF motif independently, resulting in 1 regression model for each expressed TFs. Hypothesis testing of estimated coefficients was performed by Wald-test with a heteroskedasticity-consistent robust covariance estimator, using the "sandwhich" package in R. TF coefficient

estimate p-values were corrected for multiple-hypothesis testing and the top significant TFs were reported (FDR q-value<1e-5).

ATAC-seq on cells treated *in vitro* was performed on three NLS-sAC clones, with (48 h) or without doxycycline, in parallel with three LacZ control lines, with (48 h) or without doxycycline, for a total of n = 12.

**Comparison of hyperactive YAP (5SA allele) and NLS-sSAC-associated RNA expression changes:** FASTQ files were acquired from the authors of Zhang et al. (Zhang et al., 2020b), each containing single-end RNA-seq reads from one of three biological replicates of MeWo cells expressing a DOX inducible vector control or hyperactive YAP, either untreated or treated with DOX. Quantification of gene expression was performed using Salmon (Patro et al., 2017) (version 1.4.0) using the seqBias flag. Sequencing reads were automatically inferred to be forward stranded by Salmon. The Salmon index was generated using kmers of length 31 from mature transcript sequences created from Ensembl gene set annotations (release 104) and the GRCh38 primary assembly using rtracklayer (version 1.50.0) (Lawrence et al., 2009), GenomicRanges (version 1.42.0) (Lawrence et al., 2013), and Biostrings (version 2.58.0) (Pages et al., 2021) in R. The whole genome was used as a decoy for selective alignment.

To measure hyperactive YAP associated changes in gene expression, we used DESeq2 (version 1.30.1) (Love et al., 2014). Transcript level counts from Salmon were summarized to gene counts using tximport (version 1.18.0) (Soneson et al., 2015) with the counts From Abundance argument set to 'lengthScaledTPM'. We modeled gene counts in MeWo cells as a linear function of YAP status (vector control vs YAP-5SA), DOX treatment, and an interaction term between YAP status and DOX treatment. The interaction coefficient corresponds to DOX-induced gene expression changes (in log base 2) in YAP-5SA cells relative to vector control.

To compare hyperactive YAP associated gene expression changes in MeWo cells to NLS-sAC associated changes in mouse cells, we identified high confidence orthologues with 1-to-1 mapping between humans and mice in the Ensembl database. We classified these genes as up- or down-regulated in each respective RNA-seq experiment (i.e., MeWo YAP-5SA vs control experiment, *in vivo* and *in vitro* NLS-sAC vs control experiments), then applied Fisher's exact test to a 2 × 2 contingency table to assess the concordance of observed changes between experiments. The expected counts per contingency table cell were computed assuming the proportion of up- and down-regulated genes in one experiment is independent from the other experiments, e.g., to get the expected number of genes downregulated in both experiments being compared, we simply multiplied the proportion of downregulated genes in the first experiment by the proportion of downregulated genes in the second experiment by the total number of genes.

**Inference and comparison of YAP and NLS-sAC activities in human melanoma cell lines:** Melanoma cell line data from the Cancer Cell Line Encyclopedia (CCLE) (Ghandi et al., 2019) were acquired from the DepMap data portal (Tsherniak et al., 2017) (release 20Q1; file names: sample_info.csv, CCLE_RNAseq_reads.csv, CCLE_mutations.csv).

Mutation data were used to exclude genetically related melanoma cell lines from the analysis. For each pair of cells that shared a conservative percentage of at least 10% of the union of their called mutations, we first prioritized the one whose DepMap_ID was listed in the sample_info file, then the one which had corresponding RNA-seq data, then the one which lacked additional information (additional_info) in the sample_info file, a field potentially indicating the cell line was derived from a parental cell line, such as through genetic modification or drug selection. Lastly, we prioritized the cell line with the most mutation calls, and in case of ties, we prioritized the cell line whose DepMap_ID ranked first alphanumerically when IDs were sorted from smallest to largest. We retained 45 of the 62 original melanoma cell lines with RNA-seq data after filtering. The retained cell line names are listed at the bottom of Figure 7C.

RNA-seq counts for the 45 melanoma cell lines were loaded into R. Genes with low counts were flagged and removed using the edgeR package's (version 3.32.1) filterByExpr function and default parameters (McCarthy et al., 2012). Read counts were normalized for differences in sequencing depth and subjected to variance stabilizing transformation using DESeq2.

Normalized transformed gene expression values were used to estimate YAP and NLS-sAC activity per cell line using the Gene Set Variation Analysis (GSVA) R package (version 1.38.2) (Hanzelmann et al., 2013). Briefly, GSVA standardizes expression values for each gene, then uses a Kolmogorov-Smirnov-like rank statistic to infer if genes in a provided gene set are relatively highly expressed, lowly expressed or not differentially expressed from genes outside the set, producing a per-sample continuous score greater than, less than, or equal to zero, respectively.

We provided GSVA with four gene sets. We used genes downregulated upon NLS-sAC induction in our *in vitro* experiments as markers of NLS-sAC activity. In one set, we included genes with a log fold-change < 0 and FDR <10% (NLS-sAC signature 1; n = 460 genes), and in another set we included genes ranked in the bottom 1% based on the Wald statistic from DESeq2 (NLS-sAC signature 2; n = 100 genes). We used genes upregulated upon YAP-5SA induction in MeWo cells as markers of YAP activity. In one set, we included genes with a log fold-change > 0 and FDR <10% (YAP signature 1; n = 470 genes), and in another set we included genes ranked in the top 1% based on the Wald statistic from DESeq 2 (YAP signature 2; n = 126 genes). GSVA was run using default parameters (method = "gsva", kcdf = "Gaussian", abs.ranking = FALSE, mx.diff = TRUE). We transformed NLS-sAC scores from GSVA to activity scores by multiplying them with −1.

To validate the robustness of our protein activity estimates, we complemented GSVA with an alternative approach. We first derived NLS-sAC and YAP activity markers by ranking genes based on their absolute Wald statistic then selecting the top 1% of genes and setting aside their log fold-changes, estimated by DESeq2 (*in vitro* NLS-sac up n = 45 genes, *in vitro* NLS-sAC down n = 55 genes, MeWo YAP-5SA up n = 107 genes, MeWo YAP-5SA down n = 19 genes). We centered the variance stabilized expression values of these genes around their mean in CCLE melanoma cell lines. We computed the log2 odds ratio between the sign of the DESeq2 log fold-changes with the sign of the centered expression values per sample. We used this log odds ratio as an indicator for protein activity per cell line,

where positive values indicated higher activity and negative values indicated lower activity (NLS-sAC signature 3 and YAP signature 3).

Clustering of melanoma cell lines in Figure 7C was derived using the consensus clustering, implemented in the ConsensusClusterPlus R package (version 1.54.0) (Wilkerson and Hayes, 2010). We applied ConsensusClusterPlus on variance stabilized gene expression values for 10,000 clustering iterations, at each iteration sampling 80% of cell lines, clustering them using Pearson's distance and Ward's linkage (ward.D2), then classifying them into two groups by cutting the resulting dendrogram at its highest banchpoint. The resulting "consensus matrix", which contains the proportion of times each pair of cells were grouped together, was clustered using Ward's linkage then used to classify cells into two final groups. The genes were similarly clustered by resampling subsets of genes for 100 iterations.

**RT-PCR—**Cell pellets were collected in RNAlater (Sigma Aldrich, #R0901) and stored at −20°C. Samples were homogenized using Qiashredder columns (Qiagen, #79656) and RNA was isolated according to specifications of the RNeasy plus mini kit (Qiagen, #74136). cDNA was made using the high-capacity RNA-to-cDNA kit (Thermo Fischer, #4387406). The Applied Biosystems Power SYBR green PCR master mix (Thermo Fischer, #4368706) was used for qPCR using the QuantStudio 6 real-time PCR instrument (Thermo Fischer). Delta delta CT analysis was performed to determine relative mRNA expression amongst samples normalized to *GapDH*. List of primers used for RT-PCR analyses is provided in Table S3.

## QUANTIFICATION AND STATISTICAL ANALYSIS

All statistical analyses were performed using GraphPad Prism 8.0 (GraphPad Software). Experiments were performed a minimum of three times, unless indicated otherwise in the figure legend. Comparison of means was performed using either an unpaired, two-tailed *t* test for two groups, or an ANOVA with Sidak correction for multiple comparisons for groups of three or more A two-sided Fisher's exact test was performed on the contingency data presented for nuclear sAC staining in melanoma primary biopsy samples. Wilson-Brown was performed to calculate sensitivity and specificity.

Binomial logistic regression was used to assess whether nuclear sAC positive melanoma (defined as >10% cells with nuclear staining by IHC) differed by Breslow thickness (Figure 1F). The response variable was the number of nuclear sAC positive samples and total samples, and the explanatory variable was Breslow thickness. Significance testing was performed using likelihood ratio test. Shaded regions represent the 95% confidence interval for percentage of nuclear sAC positive observations at each level of Breslow thickness.

The statistical details of experiments are provided in the figure legends, and include the statistical tests used, exact value of n and what n represents. Data is represented as mean ± SEM, unless indicated otherwise in the figure legend.

## Supplementary Material

Refer to Web version on PubMed Central for supplementary material.

## ACKNOWLEDGMENTS

We thank members of the Zippin lab for critical reading of the manuscript and Paul Christos (Weill Cornell Medical College) for independent analysis of the statistics of the manuscript. We thank Dr. Jedd Wolchok for support for this work. We thank the following people for providing cell lines for this work: SCC12 were provided by Dr. Loraine Gudas (Weill Cornell Medical College, New York, NY, USA), colon cancer lines (DLD1 and SW480) were provided by Dr. Lukas Edward Dow (Weill Cornell Medical College, New York, NY, USA), pancreatic cancer lines (Hs766t, PANC1, MIAPaCa2) were provided by Dr. Lewis Cantley (Weill Cornell Medical College, New York, NY, USA), prostate cancer cell line LNCaP was provided by Dr. Christopher Barbieri (Weill Cornell Medical College, New York, NY, USA), and the melanoma M263 line was provided by Dr. Roger Lo (UCLA Medical Center). We thank Dr. Lukas Edward Dow for providing shRNA constructs against YAP and TAZ. We thank Peter T. Meinke of the Tri-Institutional Therapeutics Discovery Institute for providing TRULI inhibitor. We thank Kieran Harvey (Peter MacCallum Cancer Centre) for YAP 5SA MeWo RNA-seq datasets. J.H.Z. was funded in part by a Melanoma Research Alliance Team Science Award, Clinique Clinical Scholars Award, American Skin Association Calder Research Scholar Award, Pfizer ASPIRE award, NCI (1 R21 CA224391-01A1), and NIAMS (1 R01 AR077664-01A1). A.S.D. was funded in part by NCI (1 F31 CA220981-01). R.A. is a recipient of the CIHR Doctoral Award - Frederick Banting and Charles Best Canada Graduate Scholarships (CGS-D). O.E. was funded in part by R01 CA194547–04, U24CA210989-03, and P50 CA211024 CORE 2. T.M. was funded in part by the NIH/NCI R01 CA215136-01A1 and Cancer Center Support Grant P30 CA008748, the Swim Across America, Ludwig Institute for Cancer Research, Parker Institute for Cancer Immunotherapy, and Breast Cancer Research Foundation. E.P. was funded in part by R00CA201228-05, MRA Young Investigator Award, Emerson Collective Cancer Research Fund, and a Feldstein Medical Foundation Grant. This research was enabled in part by support provided by Calcul Québec (https://www.calculquebec.ca/), SHARCNET (https://www.sharcnet.ca/), and Compute Canada (www.computecanada.ca)

## REFERENCES

Abbas O, Miller DD, and Bhawan J (2014). Cutaneous malignant melanoma: update on diagnostic and prognostic biomarkers. Am. J. Dermatopathol 36, 363–379. 10.1097/DAD.0b013e31828a2ec5. [PubMed: 24803061]

Acin-Perez R, Salazar E, Brosel S, Yang H, Schon EA, and Manfredi G (2009a). Modulation of mitochondrial protein phosphorylation by soluble adenylyl cyclase ameliorates cytochrome oxidase defects. EMBO Mol. Med 1, 392–406. 10.1002/emmm.200900046. [PubMed: 20049744]

Acin-Perez R, Salazar E, Kamenetsky M, Buck J, Levin LR, and Manfredi G (2009b). Cyclic AMP produced inside mitochondria regulates oxidative phosphorylation. Cell Metab. 9, 265–276. 10.1016/j.cmet.2009.01.012. [PubMed: 19254571]

Baljinnyam E, De Lorenzo MS, Xie LH, Iwatsubo M, Chen S, Goydos JS, Nowycky MC, and Iwatsubo K (2010). Exchange protein directly activated by cyclic AMP increases melanoma cell migration by a Ca2+-dependent mechanism. Cancer Res. 70, 5607–5617, Epub 2010 Jun 15. 10.1158/0008-5472.can-10-0056. [PubMed: 20551063]

Barnhill RL, Busam KJ, and Piepkorn MW (2013). Pathology of Melanocytic Nevi and Melanoma (Springer). 10.1007/978-3-642-38385-4.

Beavo JA, and Brunton LL (2002). Cyclic nucleotide research - still expanding after half a century. Nat. Rev. Mol. Cell Biol 3, 710–718. 10.1038/nrm911. [PubMed: 12209131]

Billiard J, Grewal SS, Lukaesko L, Stork PJ, and Rotwein P (2001). Hormonal control of insulin-like growth factor I gene transcription in human osteoblasts: dual actions of cAMP-dependent protein kinase on CCAAT/enhancer-binding protein delta. J. Biol. Chem 276, 31238–31246. 10.1074/jbc.M103634200. [PubMed: 11390399]

Buck J, Sinclair ML, Schapal L, Cann MJ, and Levin LR (1999). Cytosolic adenylyl cyclase defines a unique signaling molecule in mammals. Proc. Natl. Acad. Sci. USA 96, 79–84. [PubMed: 9874775]

Chang JC, and Oude-Elferink RPJ (2014). Role of the bicarbonate-responsive soluble adenylyl cyclase in pH sensing and metabolic regulation. Front. Physiol 5, 42. 10.3389/fphys.2014.00042. [PubMed: 24575049]

Chen Y, Cann MJ, Litvin TN, Iourgenko V, Sinclair ML, Levin LR, and Buck J (2000). Soluble adenylyl cyclase as an evolutionarily conserved bicarbonate sensor. Science 289, 625–628. [PubMed: 10915626]

Coles GL, Cristea S, Webber JT, Levin RS, Moss SM, He A, Sangodkar J, Hwang YC, Arand J, Drainas AP, et al. (2020). Unbiased proteomic profiling uncovers a targetable GNAS/PKA/PP2A axis in small cell lung cancer stem cells. Cancer Cell 38, 129–143.e7. 10.1016/j.ccell.2020.05.003. [PubMed: 32531271]

Cooper DMF, and Crossthwaite AJ (2006). Higher-order organization and regulation of adenylyl cyclases. Trends Pharmacol. Sci 27, 426–431. 10.1016/j.tips.2006.06.002. [PubMed: 16820220]

Cooper DMF, and Tabbasum VG (2014). Adenylate cyclase-centred microdomains. Biochem. J 462, 199–213. 10.1042/BJ20140560. [PubMed: 25102028]

Corces MR, Granja JM, Shams S, Louie BH, Seoane JA, Zhou W, Silva TC, Groeneveld C, Wong CK, Cho SW, et al. (2018). The chromatin accessibility landscape of primary human cancers. Science 362, eaav1898. 10.1126/science.aav1898. [PubMed: 30361341]

Corces MR, Trevino AE, Hamilton EG, Greenside PG, Sinnott-Armstrong NA, Vesuna S, Satpathy AT, Rubin AJ, Montine KS, Wu B, et al. (2017). An improved ATAC-seq protocol reduces background and enables interrogation of frozen tissues. Nat. Methods 14, 959–962. 10.1038/nmeth.4396. [PubMed: 28846090]

Dang CV, and Lee WM (1988). Identification of the human c-myc protein nuclear translocation signal. Mol. Cell Biol 8, 4048–4054. 10.1128/MCB.8.10.4048. [PubMed: 3054508]

Dasgupta I, and McCollum D (2019). Control of cellular responses to mechanical cues through YAP/TAZ regulation. J. Biol. Chem 294, 17693–17706. 10.1074/jbc.REV119.007963. [PubMed: 31594864]

Desman G, and Barnhill RL (2016). Barnhill's Dermatopathology Challenge: Self-Assessment & Review (McGraw-Hill Education).

Desman G, Waintraub C, and Zippin JH (2014). Investigation of cAMP microdomains as a path to novel cancer diagnostics. Biochim. Biophys. Acta 1842, 2636–2645. 10.1016/j.bbadis.2014.08.016. [PubMed: 25205620]

DiPilato LM, and Zhang J (2009). The role of membrane microdomains in shaping beta2-adrenergic receptor-mediated cAMP dynamics. Mol. Biosyst 5, 832–837. 10.1039/b823243a. [PubMed: 19603118]

Ege N, Dowbaj AM, Jiang M, Howell M, Hooper S, Foster C, Jenkins RP, and Sahai E (2018). Quantitative analysis reveals that actin and src-family kinases regulate nuclear YAP1 and its export. Cell Syst. 6, 692–708.e13. 10.1016/j.cels.2018.05.006. [PubMed: 29909276]

Elosegui-Artola A, Andreu I, Beedle AEM, Lezamiz A, Uroz M, Kosmalska AJ, Oria R, Kechagia JZ, Rico-Lastres P, Le Roux AL, et al. (2017). Force Triggers YAP nuclear entry by regulating Transport across nuclear pores. Cell 171, 1397–1410.e14. 10.1016/j.cell.2017.10.008. [PubMed: 29107331]

Fajardo AM, Piazza GA, and Tinsley HN (2014). The role of cyclic nucleotide signaling pathways in cancer: targets for prevention and treatment. Cancers 6, 436–458. 10.3390/cancers6010436. [PubMed: 24577242]

Franklin JM, Ghosh RP, Shi Q, Reddick MP, and Liphardt JT (2020). Concerted localization-resets precede YAP-dependent transcription. Nat. Commun 11, 4581. 10.1038/s41467-020-18368-x. [PubMed: 32917893]

Fu S-C, Huang H-C, Horton P, and Juan H-F (2013). ValidNESs: a database of validated leucine-rich nuclear export signals. Nucleic Acids Res. 41, D338–D343. 10.1093/nar/gks936. [PubMed: 23093589]

Gaspar JM (2018). NGmerge: merging paired-end reads via novel empirically-derived models of sequencing errors. BMC Bioinf. 19, 536. 10.1186/s12859-018-2579-2.

Ghandi M, Huang FW, Jané-Valbuena J, Kryukov GV, Lo CC, McDonald ER 3rd, Barretina J, Gelfand ET, Bielski CM, Li H, et al. (2019). Next-generation characterization of the cancer cell line Encyclopedia. Nature 569, 503–508. 10.1038/s41586-019-1186-3. [PubMed: 31068700]

Goding CR, and Arnheiter H (2019). MITF-the first 25 years. Genes Dev. 33, 983–1007. 10.1101/gad.324657.119. [PubMed: 31123060]

Grannas K, Arngården L, Lönn P, Mazurkiewicz M, Blokzijl A, Zieba A, and Söderberg O (2015). Crosstalk between hippo and TGFbeta: subcellular localization of YAP/TAZ/smad complexes. J. Mol. Biol 427, 3407–3415. 10.1016/j.jmb.2015.04.015. [PubMed: 25937570]

Hänzelmann S, Castelo R, and Guinney J (2013). GSVA: gene set variation analysis for microarray and RNA-seq data. BMC Bioinf. 14, 7. 10.1186/1471-2105-14-7.

Hoek KS, Schlegel NC, Brafford P, Sucker A, Ugurel S, Kumar R, Weber BL, Nathanson KL, Phillips DJ, Herlyn M, et al. (2006). Metastatic potential of melanomas defined by specific gene expression profiles with no BRAF signature. Pigment Cell Res. 19, 290–302. 10.1111/j.1600-0749.2006.00322.x. [PubMed: 16827748]

Hsiao JJ, and Fisher DE (2014). The roles of microphthalmia-associated transcription factor and pigmentation in melanoma. Arch. Biochem. Biophys 563, 28–34. 10.1016/j.abb.2014.07.019. [PubMed: 25111671]

Johannessen CM, Johnson LA, Piccioni F, Townes A, Frederick DT, Donahue MK, Narayan R, Flaherty KT, Wargo JA, Root DE, and Garraway LA (2013). A melanocyte lineage program confers resistance to MAP kinase pathway inhibition. Nature 504, 138–142. 10.1038/nature12688. [PubMed: 24185007]

Kastan N, Gnedeva K, Alisch T, Petelski AA, Huggins DJ, Chiaravalli J, Aharanov A, Shakked A, Tzahor E, Nagiel A, et al. (2021). Small-molecule inhibition of Lats kinases may promote Yap-dependent proliferation in postmitotic mammalian tissues. Nat. Commun 12, 3100. 10.1038/s41467-021-23395-3. [PubMed: 34035288]

Kim M, Kim M, Lee S, Kuninaka S, Saya H, Lee H, Lee S, and Lim DS (2013). cAMP/PKA signalling reinforces the LATS-YAP pathway to fully suppress YAP in response to actin cytoskeletal changes. EMBO J. 32, 1543–1555. 10.1038/emboj.2013.102. [PubMed: 23644383]

Kloster MM, Hafte TT, Moltzau LR, Naderi EH, Dahle MK, Skålhegg BS, Gaudernack G, Levy FO, Naderi S, and Blomhoff HK (2008). EBV infection renders B cells resistant to growth inhibition via adenylyl cyclase. Cell. Signal 20, 1169–1178. 10.1016/j.cellsig.2008.02.007. [PubMed: 18406106]

Koo JH, and Guan KL (2018). Interplay between YAP/TAZ and metabolism. Cell Metab. 28, 196–206. 10.1016/j.cmet.2018.07.010. [PubMed: 30089241]

Lawrence M, Gentleman R, and Carey V (2009). rtracklayer: an R package for interfacing with genome browsers. Bioinformatics 25, 1841–1842. 10.1093/bioinformatics/btp328. [PubMed: 19468054]

Lawrence M, Huber W, Pagès H, Aboyoun P, Carlson M, Gentleman R, Morgan MT, and Carey VJ (2013). Software for computing and annotating genomic ranges. PLoS Comput. Biol 9, e1003118. 10.1371/journal.pcbi.1003118. [PubMed: 23950696]

Lee D, and Hong JH (2020). The fundamental role of bicarbonate Transporters and associated carbonic anhydrase enzymes in maintaining ion and pH homeostasis in non-secretory organs. Int. J. Mol. Sci 21, E339. 10.3390/ijms21010339. [PubMed: 31947992]

Li H, Kim SM, Savkovic V, Jin SA, Choi YD, and Yun SJ (2016). Expression of soluble adenylyl cyclase in acral melanomas. Clin. Exp. Dermatol 41, 425–429. 10.1111/ced.12730. [PubMed: 26290224]

Li W, Cooper J, Zhou L, Yang C, Erdjument-Bromage H, Zagzag D, Snuderl M, Ladanyi M, Hanemann CO, Zhou P, et al. (2014). Merlin/NF2 loss-driven tumorigenesis linked to CRL4(DCAF1)-mediated inhibition of the hippo pathway kinases Lats1 and 2 in the nucleus. Cancer Cell 26, 48–60. 10.1016/j.ccr.2014.05.001. [PubMed: 25026211]

Liberti MV, and Locasale JW (2016). The warburg effect: how does it benefit cancer cells? Trends Biochem. Sci 41, 211–218. 10.1016/j.tibs.2015.12.001. [PubMed: 26778478]

Lohse C, Bock A, Maiellaro I, Hannawacker A, Schad LR, Lohse MJ, and Bauer WR (2017). Experimental and mathematical analysis of cAMP nanodomains. PLoS One 12, e0174856. 10.1371/journal.pone.0174856. [PubMed: 28406920]

Love MI, Huber W, and Anders S (2014). Moderated estimation of fold change and dispersion for RNA-seq data with DESeq2. Genome Biol. 15, 550. 10.1186/s13059-014-0550-8. [PubMed: 25516281]

Love MI, Soneson C, Hickey PF, Johnson LK, Pierce NT, Shepherd L, Morgan M, and Patro R (2020). Tximeta: reference sequence checksums for provenance identification in RNA-seq. PLoS Comput. Biol 16, e1007664. 10.1371/journal.pcbi.1007664. [PubMed: 32097405]

Lyons J, Bastian BC, and McCormick F (2013). MC1R and cAMP signaling inhibit cdc25B activity and delay cell cycle progression in melanoma cells. Proc. Natl. Acad. Sci. USA 110, 13845–13850. 10.1073/pnas.1201917110. [PubMed: 23908401]

Magro CM, Crowson AN, Desman G, and Zippin JH (2012). Soluble adenylyl cyclase antibody profile as a diagnostic adjunct in the assessment of pigmented lesions. Arch. Dermatol 148, 335–344. 10.1001/archdermatol.2011.338. [PubMed: 22105816]

Manning SA, Dent LG, Kondo S, Zhao ZW, Plachta N, and Harvey KF (2018). Dynamic fluctuations in subcellular localization of the hippo pathway effector yorkie in vivo. Curr. Biol 28, 1651–1660.e4. 10.1016/j.cub.2018.04.018. [PubMed: 29754899]

Marino ML, Pellegrini P, Di Lernia G, Djavaheri-Mergny M, Brnjic S, Zhang X, Hägg M, Linder S, Fais S, Codogno P, and De Milito A (2012). Autophagy isaprotective mechanism for human melanomacells under acidic stress. J. Biol. Chem 287, 30664–30676. 10.1074/jbc.M112.339127. [PubMed: 22761435]

McCarthy DJ, Chen Y, and Smyth GK (2012). Differential expression analysis of multifactor RNA-Seq experiments with respect to biological variation. Nucleic Acids Res. 40, 4288–4297. 10.1093/nar/gks042. [PubMed: 22287627]

Michalides R, Griekspoor A, Balkenende A, Verwoerd D, Janssen L, Jalink K, Floore A, Velds A, van't Veer L, and Neefjes J (2004). Tamoxifen resistance by a conformational arrest of the estrogen receptor alpha after PKA activation in breast cancer. Cancer Cell 5, 597–605. 10.1016/j.ccr.2004.05.016. [PubMed: 15193262]

Musheshe N, Schmidt M, and Zaccolo M (2018). cAMP: from long-range second messenger to nanodomain signalling. Trends Pharmacol. Sci 39, 209–222. 10.1016/j.tips.2017.11.006. [PubMed: 29289379]

Paek SC, Griffith KA, Johnson TM, Sondak VK, Wong SL, Chang AE, Cimmino VM, Lowe L, Bradford CR, Rees RS, and Sabel MS (2007). The impact of factors beyond breslow depth on predicting sentinel lymph node positivity in melanoma. Cancer 109, 100–108. 10.1002/cncr.22382. [PubMed: 17146784]

Pages H, Aboyoun P, Gentleman R, and DebRoy S (2021). Biostrings: efficient manipulation of biological strings. R package version 2.60.1

Passaniti A, Brusgard JL, Qiao Y, Sudol M, and Finch-Edmondson M (2017). Advances in Experimental Medicine and Biology.

Patra KC, Kato Y, Mizukami Y, Widholz S, Boukhali M, Revenco I, Grossman EA, Ji F, Sadreyev RI, Liss AS, et al. (2018). Mutant GNAS drives pancreatic tumourigenesis by inducing PKA-mediated SIK suppression and reprogramming lipid metabolism. Nat. Cell Biol 20, 811–822. 10.1038/s41556-018-0122-3. [PubMed: 29941929]

Patro R, Duggal G, Love MI, Irizarry RA, and Kingsford C (2017). Salmon provides fast and bias-aware quantification of transcript expression. Nat. Methods 14, 417–419. 10.1038/nmeth.4197. [PubMed: 28263959]

Pauli C, Hopkins BD, Prandi D, Shaw R, Fedrizzi T, Sboner A, Sailer V, Augello M, Puca L, Rosati R, et al. (2017). Personalized in vitro and in vivo cancer models to guide precision medicine. Cancer Discov. 7, 462–477. 10.1158/2159-8290.CD-16-1154. [PubMed: 28331002]

Ramos-Espiritu L, Diaz A, Nardin C, Saviola AJ, Shaw F, Plitt T, Yang X, Wolchok J, Pirog EC, Desman G, et al. (2016). The metabolic/pH sensor soluble adenylyl cyclase is a tumor suppressor protein. Oncotarget 7, 45597–45607. 10.18632/oncotarget.10056. [PubMed: 27323809]

Rehmann H, Wittinghofer A, and Bos JL (2007). Capturing cyclic nucleotides in action: snapshots from crystallographic studies. Nat. Rev. Mol. Cell Biol 8, 63–73. 10.1038/nrm2082. [PubMed: 17183361]

Sample V, DiPilato LM, Yang JH, Ni Q, Saucerman JJ, and Zhang J (2012). Regulation of nuclear PKA revealed by spatiotemporal manipulation of cyclic AMP. Nat. Chem. Biol 8, 375–382. 10.1038/nchembio.799. [PubMed: 22366721]

Sassone-Corsi P (2012). The cyclic AMP pathway. Cold Spring Harb. Perspect. Biol 4, a011148. 10.1101/cshperspect.a011148. [PubMed: 23209152]

Schep AN, Buenrostro JD, Denny SK, Schwartz K, Sherlock G, and Greenleaf WJ (2015). Structured nucleosome fingerprints enable high-resolution mapping of chromatin architecture within regulatory regions. Genome Res. 25, 1757–1770. 10.1101/gr.192294.115. [PubMed: 26314830]

Schep AN, Wu B, Buenrostro JD, and Greenleaf WJ (2017). chromVAR: inferring transcription-factor-associated accessibility from single-cell epigenomic data. Nat. Methods 14, 975–978. 10.1038/nmeth.4401. [PubMed: 28825706]

Schneider CA, Rasband WS, and Eliceiri KW (2012). NIH Image to ImageJ: 25 years of image analysis. Nat Methods. 9, 671–675. 10.1038/nmeth.2089. [PubMed: 22930834]

Shashikant T, and Ettensohn CA (2019). Genome-wide analysis of chromatin accessibility using ATAC-seq. Methods Cell Biol. 151, 219–235. 10.1016/bs.mcb.2018.11.002. [PubMed: 30948010]

Sheppard JR, Koestler TP, Corwin SP, Buscarino C, Doll J, Lester B, Greig RG, and Poste G (1984). Experimental metastasis correlates with cyclic AMP accumulation in B16 melanoma clones. Nature 308, 544–547. [PubMed: 6323999]

Shreberk-Shaked M, and Oren M (2019). New insights into YAP/TAZ nucleo-cytoplasmic shuttling: new cancer therapeutic opportunities? Mol. Oncol 13, 1335–1341. 10.1002/1878-0261.12498. [PubMed: 31050214]

Smith FD, Esseltine JL, Nygren PJ, Veesler D, Byrne DP, Vonderach M, Strashnov I, Eyers CE, Eyers PA, Langeberg LK, and Scott JD (2017). Local protein kinase A action proceeds through intact holoenzymes. Science 356, 1288–1293. 10.1126/science.aaj1669. [PubMed: 28642438]

Solky AC, and Zembowicz A (2014). Soluble adenylyl cyclase antibody (R21)as a diagnostic adjunct in the evaluation of lentigo maligna margins during slow mohs surgery. Am. J. Dermatopathol 36, 882–887. 10.1097/DAD.0000000000000074. [PubMed: 24698940]

Soneson C, Love MI, and Robinson MD (2015). Differential analyses for RNA-seq: transcript-level estimates improve gene-level inferences. F1000Res. 4, 1521. 10.12688/f1000research.7563.2. [PubMed: 26925227]

Spencer NY, and Stanton RC (2019). The warburg effect, lactate, and nearly a century of trying to cure cancer. Semin. Nephrol 39, 380–393. 10.1016/j.semnephrol.2019.04.007. [PubMed: 31300093]

Torres-Quesada O, Mayrhofer JE, and Stefan E (2017). The many faces of compartmentalized PKA signalosomes. Cell. Signal 37, 1–11. 10.1016/j.cellsig.2017.05.012. [PubMed: 28528970]

Tresguerres M, Levin LR, and Buck J (2011). Intracellular cAMP signaling by soluble adenylyl cyclase. Kidney Int. 79, 1277–1288. 10.1038/ki.2011.95. [PubMed: 21490586]

Tsherniak A, Vazquez F, Montgomery PG, Weir BA, Kryukov G, Cowley GS, Gill S, Harrington WF, Pantel S, Krill-Burger JM, et al. (2017). Defining a cancer dependency map. Cell 170, 564–576.e16. 10.1016/j.cell.2017.06.010. [PubMed: 28753430]

Valsecchi F, Konrad C, D'Aurelio M, Ramos-Espiritu LS, Stepanova A, Burstein SR, Galkin A, Magranè J, Starkov A, Buck J, et al. (2017). Distinct intracellular sAC-cAMP domains regulate ER Ca(2+) signaling and OXPHOS function. J. Cell Sci 130, 3713–3727. 10.1242/jcs.206318. [PubMed: 28864766]

Wang X, Cai B, Yang X, Sonubi OO, Zheng Z, Ramakrishnan R, Shi H, Valenti L, Pajvani UB, Sandhu J, et al. (2020). Cholesterol stabilizes TAZ in hepatocytes to promote experimental non-alcoholic steatohepatitis. Cell Metab. 31, 969–986.e7. 10.1016/j.cmet.2020.03.010. [PubMed: 32259482]

Wen W, Meinkoth JL, Tsien RY, and Taylor SS (1995). Identification of a signal for rapid export of proteins from the nucleus. Cell 82, 463–473. 10.1016/0092-8674(95)90435-2. [PubMed: 7634336]

Wilkerson MD, and Hayes DN (2010). ConsensusClusterPlus: a class discovery tool with confidence assessments and item tracking. Bioinformatics 26, 1572–1573. 10.1093/bioinformatics/btq170. [PubMed: 20427518]

Yu FX, Zhang Y, Park HW, Jewell JL, Chen Q, Deng Y, Pan D, Taylor SS, Lai ZC, and Guan KL (2013). Protein kinase A activates the Hippo pathway to modulate cell proliferation and differentiation. Genes Dev. 27, 1223–1232. 10.1101/gad.219402.113. [PubMed: 23752589]

Yu F-X, Zhao B, and Guan K-L (2015). Hippo pathway in organ size control, tissue homeostasis, and cancer. Cell 163, 811–828. 10.1016/j.cell.2015.10.044. [PubMed: 26544935]

Yu FX, Zhao B, Panupinthu N, Jewell JL, Lian I, Wang LH, Zhao J, Yuan H, Tumaneng K, Li H, et al. (2012). Regulation of the Hippo-YAP pathway by G-protein-coupled receptor signaling. Cell 150, 780–791. 10.1016/j.cell.2012.06.037. [PubMed: 22863277]

Zaccolo M (2011). Spatial control of cAMP signalling in health and disease. Curr. Opin. Pharmacol 11, 649–655. 10.1016/j.coph.2011.09.014. [PubMed: 22000603]

Zanconato F, Cordenonsi M, and Piccolo S (2019). YAP and TAZ: a signalling hub of the tumour microenvironment. Nat. Rev. Cancer 19, 454–464. 10.1038/s41568-019-0168-y. [PubMed: 31270418]

Zhang JZ, Lu TW, Stolerman LM, Tenner B, Yang JR, Zhang JF, Falcke M, Rangamani P, Taylor SS, Mehta S, and Zhang J (2020a). Phase separation of a PKA regulatory subunit controls cAMP compartmentation and oncogenic signaling. Cell 182, 1531–1544.e15. 10.1016/j.cell.2020.07.043. [PubMed: 32846158]

Zhang X, Yang L, Szeto P, Abali GK, Zhang Y, Kulkarni A, Amarasinghe K, Li J, Vergara IA, Molania R, et al. (2020b). The Hippo pathway oncoprotein YAP promotes melanoma cell invasion and spontaneous metastasis. Oncogene 39, 5267–5281. 10.1038/s41388-020-1362-9. [PubMed: 32561850]

Zhang X, Zhao H, Li Y, Xia D, Yang L, Ma Y, and Li H (2018). The role of YAP/TAZ activity in cancer metabolic reprogramming. Mol. Cancer 17, 134. 10.1186/s12943-018-0882-1. [PubMed: 30176928]

Zhao B, Li L, Tumaneng K, Wang CY, and Guan KL (2010). A coordinated phosphorylation by Lats and CK1 regulates YAP stability through SCF(beta-TRCP). Genes Dev. 24, 72–85. 10.1101/gad.1843810. [PubMed: 20048001]

Zhao B, Wei X, Li W, Udan RS, Yang Q, Kim J, Xie J, Ikenoue T, Yu J, Li L, et al. (2007). Inactivation of YAP oncoprotein by the Hippo pathway is involved in cell contact inhibition and tissue growth control. Genes Dev. 21, 2747–2761. 10.1101/gad.1602907. [PubMed: 17974916]

Zhou D, Ota K, Nardin C, Feldman M, Widman A, Wind O, Simon A, Reilly M, Levin LR, Buck J, et al. (2018). Mammalian pigmentation is regulated by a distinct cAMP-dependent mechanism that controls melanosome pH. Sci. Signal 11, eaau7987. [PubMed: 30401788]

Zhou Y, Huang T, Cheng ASL, Yu J, Kang W, and To KF (2016). The TEAD family and its oncogenic role in promoting tumorigenesis. Int. J. Mol. Sci 17, E138. 10.3390/ijms17010138. [PubMed: 26805820]

Zhu A, Ibrahim JG, and Love MI (2019). Heavy-tailed prior distributions for sequence count data: removing the noise and preserving large differences. Bioinformatics 35, 2084–2092. 10.1093/bioinformatics/bty895. [PubMed: 30395178]

Zhu J, and Thompson CB (2019). Metabolic regulation of cell growth and proliferation. Nat. Rev. Mol. Cell Biol 20, 436–450. 10.1038/s41580-019-0123-5. [PubMed: 30976106]

Zippin JH, Chen Y, Straub SG, Hess KC, Diaz A, Lee D, Tso P, Holz GG, Sharp GWG, Levin LR, and Buck J (2013). CO2/HCO3(−)- and calcium-regulated soluble adenylyl cyclase as a physiological ATP sensor. J. Biol. Chem 288, 33283–33291.10.1074/jbc.M113.510073. [PubMed: 24100033]

Zippin JH, Farrell J, Huron D, Kamenetsky M, Hess KC, Fischman DA, Levin LR, and Buck J (2004). Bicarbonate-responsive "soluble" adenylyl cyclase defines a nuclear cAMP microdomain. J. Cell Biol 164, 527–534. 10.1083/jcb.200311119. [PubMed: 14769862]

Zippin JH, Levin LR, and Buck J (2001). CO(2)/HCO(3)(−)-responsive soluble adenylyl cyclase as a putative metabolic sensor. Trends Endocrinol. Metab 12, 366–370. [PubMed: 11551811]

## Highlights

- Four spatially distinct sources of cAMP induce unique gene-expression profiles
- Nuclear cAMP is tumor suppressive in a wide range of cancers
- Nuclear cAMP inhibits YAP by inducing phosphorylation only at serine 397
- Nuclear cAMP drives export of YAP from the nucleus without affecting YAP stability

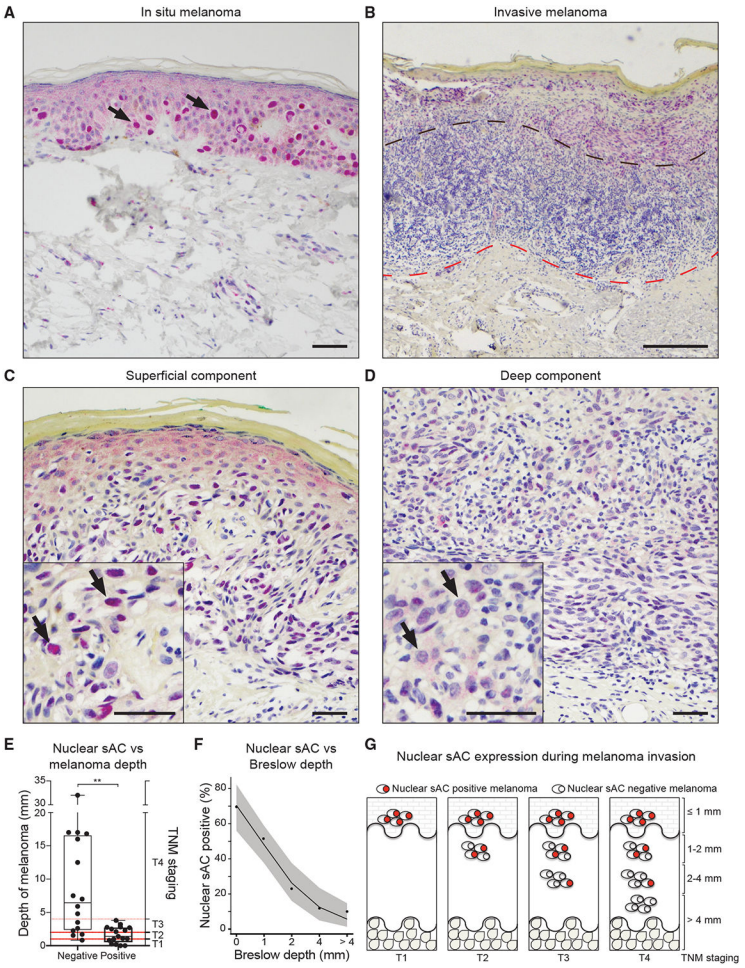


**Figure 1. A nuclear cAMP microdomain is lost upon melanoma invasion**

(A) Subcellular sAC localization in *in situ* human melanoma; arrows point to examples of nuclear sAC-positive cells. Scale bar: 50 μm.

(B) Loss of nuclear sAC upon deep dermal invasion; black line denotes transition from superficial to deep melanoma component, while red line marks the leading edge of the tumor. Scale bar: 500 μm.

(C) Maintenance of nuclear sAC in superficial component of invasive melanoma (indicated by arrows). Scale bars: 25 μm.

(D) Loss of nuclear sAC in the deep dermal component of invasive melanoma (indicated by arrows). Scale bars: 50 μm.

(E) Correlation between melanoma depth and the presence of nuclear sAC-positive melanocytes. Welch's t test; **p ≤ 0.01. Box extends from 25$^{th}$ to 75$^{th}$ percentiles, with median indicated inside. Whiskers extend from minimum to maximum value with individual data points shown. n = 34 individual melanoma biopsies.

(F) Increasing Breslow depth correlates with loss of nuclear sAC-positive cells in human melanoma. Points represent observed values (%), and solid line represents regression model estimates with 95% confidence interval (CI) as shaded regions. Significance testing ($p < 0.001$) was performed using likelihood-ratio test.

(G) Schematic of nuclear sAC expression during different stages of melanoma invasion.

See also Table S1.

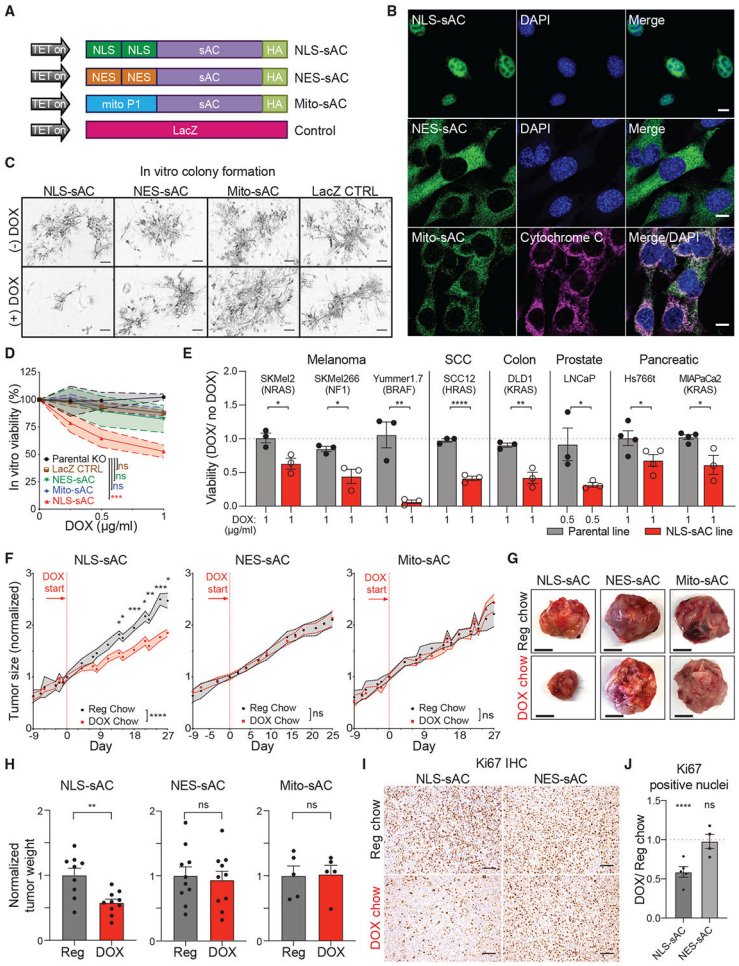


**Figure 2. The nuclear cAMP microdomain suppresses tumor growth *in vitro* and *in vivo***

(A) cDNA schematics of sAC cAMP microdomain constructs. NLS, nuclear localization signal; NES, nuclear export signal; mito P1, mitochondrial P1 localization signal; LacZ, beta galactosidase encoding gene; TET on, doxycycline-activated promoter; HA, hemagglutinin tag.

(B) Microscopy images of melanoma clones showing targeted localization of sAC as detected with anti-HA antibody (green). DAPI (blue) used to label nuclei. Anticytochrome c antibody (magenta) used to label mitochondria. Scale bar: 10 µm.

(C) *In vitro* colony formation by mouse melanoma cells in Matrigel after 7 days ± doxycycline (DOX; 1 µg/mL). Scale bar: 100 µm.

(D) Viability, based on relative ATP, of mouse melanoma colonies as in (C). n = 3 or more biological replicates; error bars, SEM; two-way ANOVA.

(E) Viability of cancer cell lines following nuclear sAC expression as in (D). Error bars, SEM; Student's t test, n = 3 biological replicates.

(F) Melanoma tumor growth ± sAC microdomain expression. Switch to DOX containing chow at arrow/red vertical line. Data normalized to day 0 (day when mice changed to DOX containing chow). Reg, regular chow, gray. Dashed lines, SEM; mixed effect ANOVA, with Sidak correction for multiple comparisons. NLS-sAC, n = 15 animals per cohort; NES-sAC and mito-sAC, n = 10 animals per cohort.

(G) Gross tumor images from (F). Scale bar: 1 cm.
(H) Weight of NLS-sAC, NES-sAC, and mito-sAC tumors from mice fed Reg (Reg, gray bars) or DOX-containing (DOX, red bars) chow. Weight was normalized to regular chow (set to 1). Error bars, SEM; Student's t test. NLS-sAC Reg, n = 9 animals; NLS-sAC DOX and NES-sAC, n = 10 animals per cohort; mito-sAC n = 5 animals per cohort.
(I) Microscopic image of Ki67 immunohistochemistry (IHC) analysis. Scale bar: 100 μm.
(J) Quantitation of Ki67-positive nuclei in tumor sections from *in vivo* experiment represented as a fold change over corresponding control cohort. Mean with data points for individual tumors are shown. NLS-sAC, n = 5 biological replicates, NES-sAC, n = 4 biological replicates. Error bars, SEM; Student's t test. (ns, $p > 0.05$; *$p \leq 0.05$; **$p \leq 0.01$; ***$p \leq 0.001$; ****$p \leq 0.0001$).
See also Figures S1-S3.

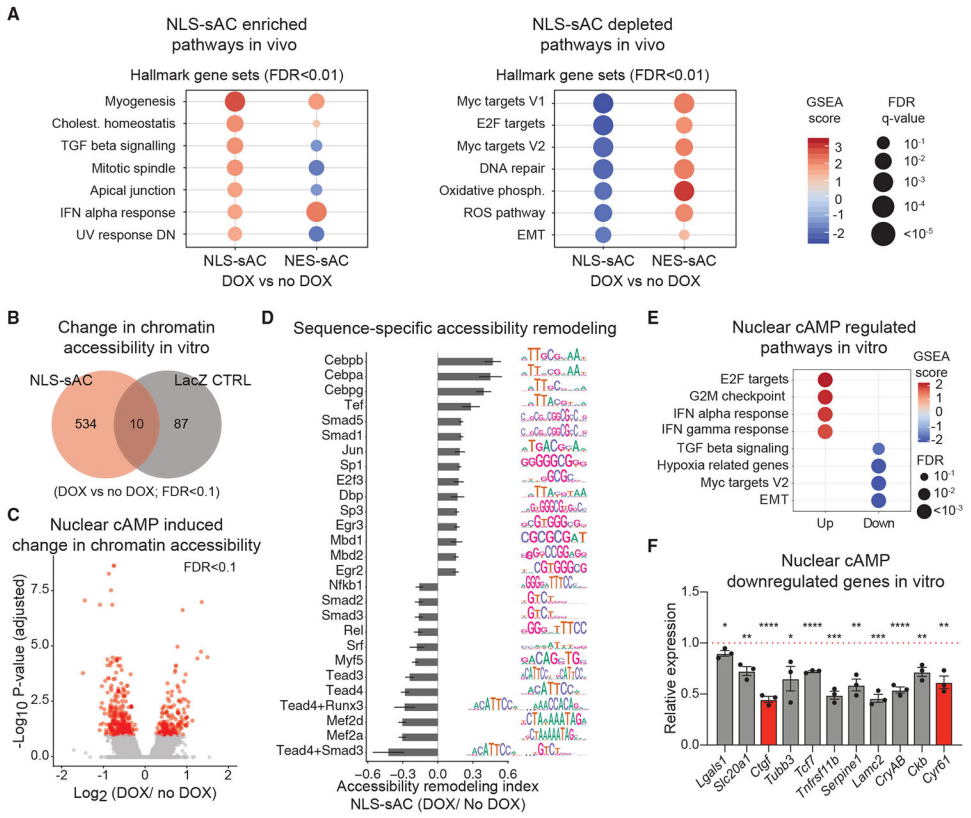


**Figure 3. The nuclear cAMP microdomain alters chromatin accessibility and inhibits pro-tumorigenic gene expression profiles via Hippo pathway**

(A) Gene set enrichment analysis (GSEA) of global expression changes in NLS-sAC- (DOX) and NES-sAC- (DOX) versus control-expressing (no DOX) tumors.

(B) Overlap of differential chromatin accessibility following NLS-sAC or LacZ expression.

(C) Volcano plot of differential chromatin accessibility of DNA elements in NLS-sAC-expressing melanoma cells.

(D) Change in transcription factor accessibility remodeling following NLS-sAC expression. The 27 most significant transcription factors (FDR $<1 \times 10^{-5}$) are reported, with their consensus motif sequence logos indicated on the right. Error bars, 95% CI.

(E) GSEA following NLS-sAC expression in mouse melanoma cells *in vitro*.

(F) RT-PCR confirmation of genes with reduced expression identified by RNA-seq in (E). n = 3 biological replicates. Hippo pathway genes labeled as red bars. Represented as DOX/no DOX. Mean values; error bars, SEM. Student's t test. (*p ≤ 0.05; **p ≤ 0.01; ***p ≤ 0.001; ****p ≤ 0.0001).

See also Figures S4-S6.

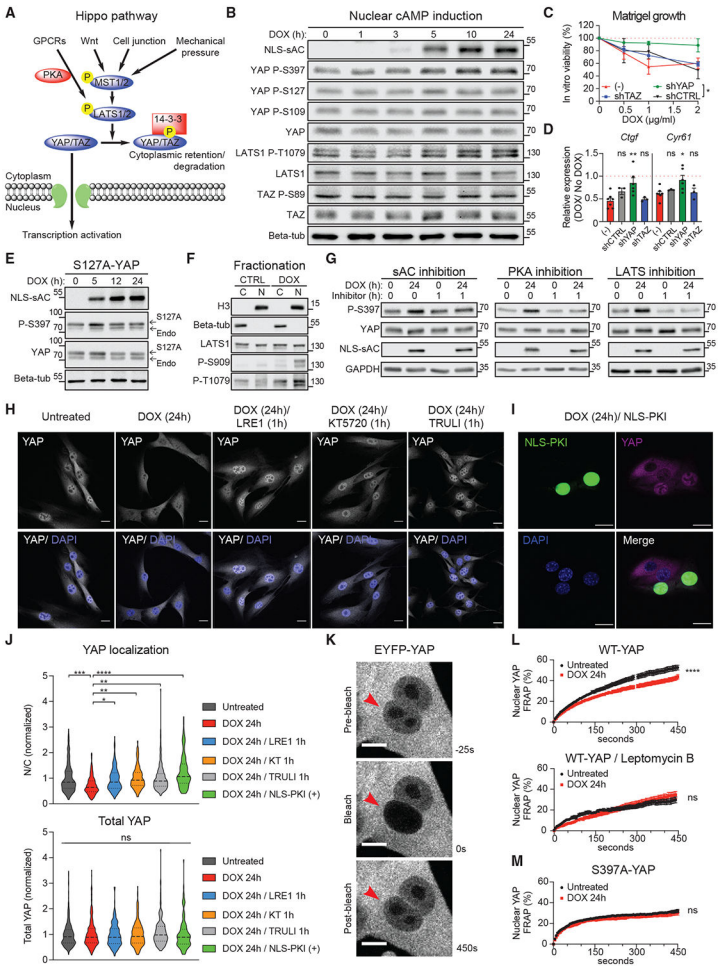


**Figure 4. The nuclear cAMP/PKA/LATS signaling cascade inhibits YAP by inducing S397 phosphorylation and nuclear export**

(A) Schematic of canonical Hippo signaling.

(B) Western blot analysis of nuclear cAMP induced phosphorylation of LATS1, YAP, and TAZ (n ≥ 3 biological replicates; representative shown).

(C) Viability of mouse melanoma colonies in Matrigel following either YAP or TAZ knockdown, assessed by ATP content. (–, red), parental cell line; (shCTRL, black), parental cell line transduced with scrambled shRNA; (shTAZ, blue); (shYAP, green). n ≥ 4 biological replicates; error bars, SEM; two-way ANOVA.

(D) NLS-sAC reduces *Ctgf* and *Cyr61* expression in parental lines (–, red) and in cells transduced with scrambled shRNA (shCTRL, gray), as measured by qRT-PCR. Knockdown of YAP (shYAP, green), but not TAZ (shTAZ, blue), abolishes nuclear cAMP effect on the expression of these genes. Expression relative to cells without DOX treatment (n ≥ 4 biological replicates; error bars, SEM; Student's t test).

(E) Phosphorylation of S397 induced by nuclear cAMP does not require S127 phosphorylation (n = 3 biological replicates; representative shown). S127A, FLAG-tagged YAP with S127 mutated to alanine; Endo, endogenous YAP.

(F) Fractionation of melanoma cells demonstrates the presence of LATS in both the cytoplasmic (C) and nuclear (N) fractions. Active LATS (phosphorylated on both S909

and T1079) is enriched in the nuclear fraction of cells after NLS-sAC expression (DOX; 24 h). Histone H3 and beta-tubulin markers for nuclear and cytoplasmic fractions, respectively (n = 3 biological replicates; representative shown).

(G) Nuclear cAMP-induced phosphorylation of YAP at S397 is abolished by treatment with the sAC inhibitor LRE1, the PKA inhibitor KT5720, and the LATS kinase inhibitor TRULI (n = 3 biological replicates; representative shown).

(H) Microscopic images showing loss of nuclear YAP upon NLS-sAC induction and inhibition of YAP nuclear loss by sAC, PKA, and LATS inhibitors (LRE, KT5720, and TRULI, respectively). Scale bar: 20 μm.

(I) Microscopic images of YAP (purple) nuclear expression following NLS-sAC expression in the presence or absence of a nucleus-targeted protein kinase A inhibitor (NLS-PKI; green). Scale bar: 20 μm.

(J) Quantification of YAP localization represented as nuclear to cytoplasmic ratio (N/C; top panel) following nuclear cAMP induction alone (DOX, 24 h) or in the presence of sAC inhibitor (LRE1), PKA inhibitors (KT5720 and NLS-PKI), or LATS inhibitor (TRULI); total YAP level for all conditions shown (bottom panel). Dashed line within each violin plot, median; dotted lines, quartiles; error bars, SEM; one-way ANOVA with Sidak's correction for multiple comparisons. n = 3–6 separate experiments. Total cell number per group: 446 untreated; 477 DOX 24 h; 221 DOX 24 h/LRE1 1 h; 252 DOX 24 h/KT5720 1 h; 212 DOX 24 h/TRULI 1 h; and 143 DOX 24 h/NLS-PKI (+).

(K) Microscopic image examples of FRAP analysis of EYFP-tagged YAP. Bleached nucleus is marked by an arrowhead. Scale bar: 10 μm.

(L) FRAP analysis of EYFP-YAP following NLS-sAC expression in the presence or absence of the nuclear export inhibitor leptomycin B (without leptomycin B: n = 3 separate experiments, 47 nuclei total per group; with leptomycin B: n = 2 separate experiments, 13 nuclei total per group; error bars, SEM; mixed effect ANOVA).

(M) FRAP analysis of EYFP-tagged YAP-S397A showing no changes in nuclear YAP recovery after NLS-sAC expression (n = 3 separate experiments, 52 untreated nuclei and 32 DOX-treated nuclei; error bars, SEM; mixed effect ANOVA). (ns, $p > 0.05$; *$p \leq 0.05$; **$p \leq 0.01$; ***$p \leq 0.001$; ****$p \leq 0.0001$).

See also Figures S7 and S8.

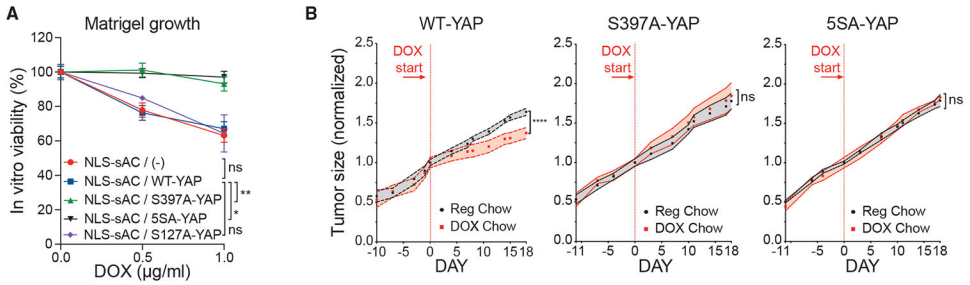


**Figure 5. Nuclear sAC inhibits tumor growth in a YAP S397 phosphorylation-dependent manner**

(A) Colony growth in Matrigel, assessed by ATP content, of the parental (−) NLS-sAC melanoma line or melanoma cells overexpressing either wild type (WT)-YAP or mutant YAPs (S127A, S397A, or 5SA). n = 6 biological replicates; error bars, SEM; ANOVA.

(B) Tumor growth following NLS-sAC induction in WT-YAP-, S397A-YAP-, or 5SA-YAP-expressing melanoma cells. Switch to DOX chow (red) is indicated by the arrow/red line. Reg, regular chow, gray. Error bars, SEM; mixed effect ANOVA, with Sidak's correction for multiple comparisons; n = 5 animals per cohort, except 5SA-YAP, where n = 4. (ns, $p > 0.05$; *$p \leq 0.05$; **$p \leq 0.01$; ***$p \leq 0.001$; ****$p \leq 0.0001$).

See also Figure S9.

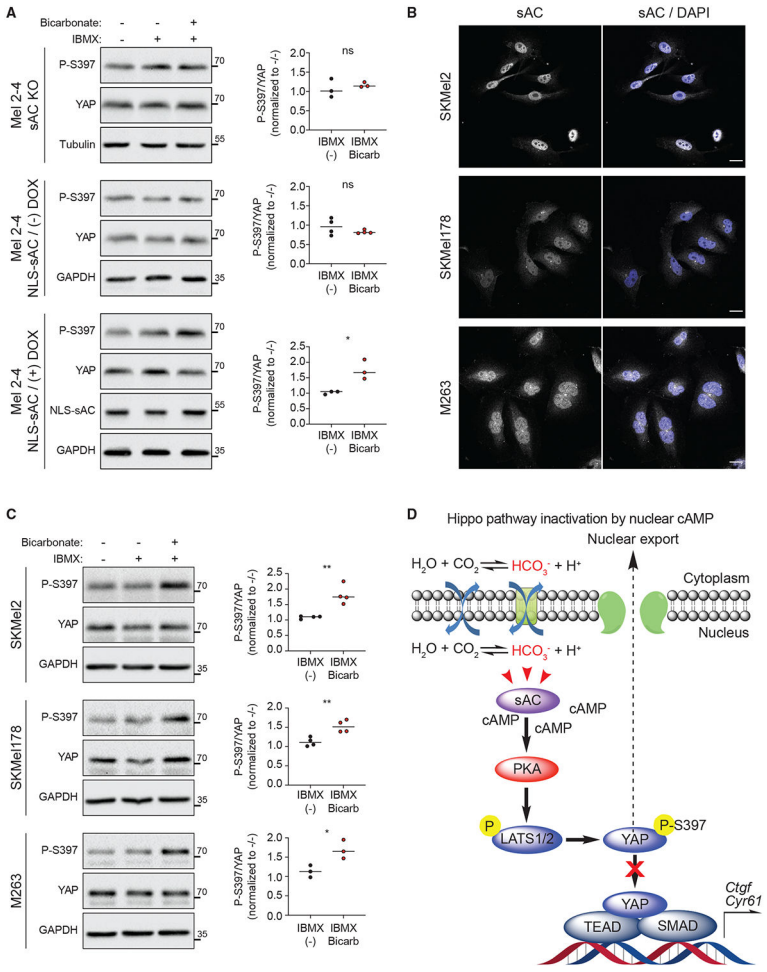


**Figure 6. The endogenous sAC agonist bicarbonate induces YAP S397 phosphorylation in melanoma**

(A) Left panel, representative western blots showing YAP S397 phosphorylation in mouse melanoma lines in response to 10 μM IBMX with or without bicarbonate ion ($HCO_3^-$), an agonist of sAC, for 30 min. Right panel, quantification of P-397 band volumes normalized to total YAP band intensity expressed as the fold change of bicarbonate + IBMX (+,+) relative to IBMX alone (−,+). n ≥ 3 biological replicates. Student's t test.

(B) Microscopy images of endogenous sAC localization in human melanoma cell lines. Scale bar: 10 μm.

(C) Left panel, representative western blots showing YAP S397 phosphorylation in human melanoma lines incubated in control media or in the presence of 50 μM IBMX with or without bicarbonate ion ($HCO_3^-$), an agonist of endogenous sAC, for 30 min. Right panel, quantification of P-397 band volumes normalized to total YAP band intensity expressed as the fold change of bicarbonate + IBMX (+,+) relative to IBMX alone (−,+). n ≥ 3 biological replicates. Student's t test.

(D) Model of Hippo pathway inhibition by nuclear cAMP. (ns, $p > 0.05$; *$p \leq 0.05$; **$p \leq 0.01$).

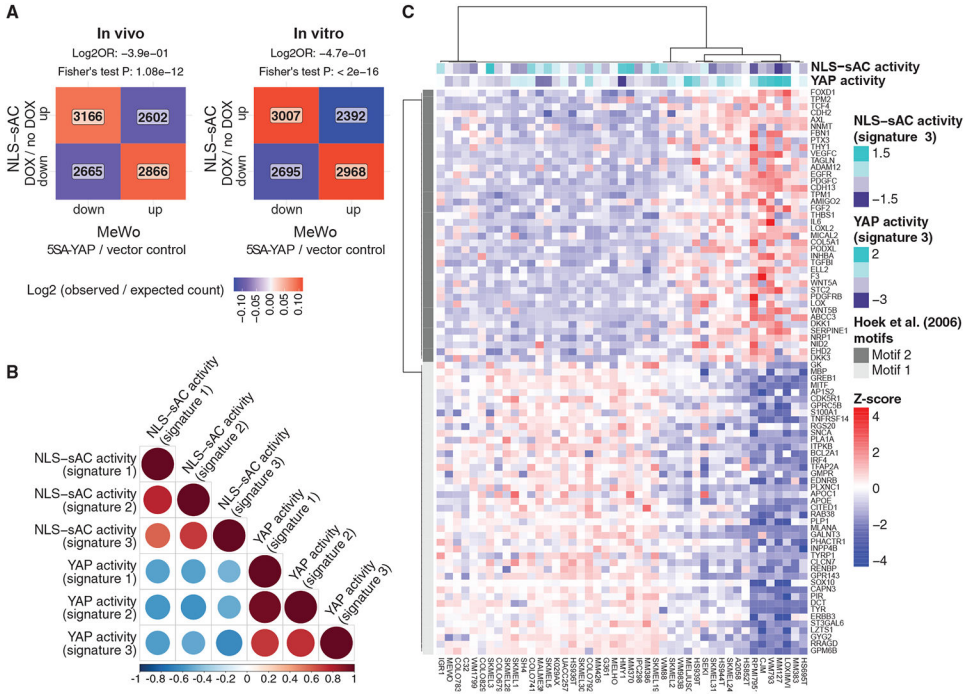


**Figure 7. Nuclear cAMP- and YAP-dependent signaling are inversely correlated in human melanoma**

(A) Heatmaps comparing the relative upregulation and downregulation of genes in hyperactive YAP-expressing MeWo cells (rows) versus NLS-sAC-expressing (columns) *in vivo* mouse melanoma tumors (left panel) and *in vitro* mouse melanoma cell lines (right panel). The number of genes observed in each quadrant is indicated.

(B) Spearman correlation between inferred NLS-sAC and YAP activities across 45 melanoma cell lines from the Cancer Cell Line Encyclopedia (CCLE). Three approaches were used to derive the activity signatures, sigs. 1–3 (see method details, genomic data analysis section).

(C) Heatmap showing Z score-transformed mRNA expression values for melanocytic and neural crest differentiation signature genes (motif 1) and transforming growth factor beta (TGF-β)-like signal signature genes (motif 2), defined by Hoek et al. (2006), in 45 melanoma cell lines (columns). Inferred NLS-sAC and YAP activities in each cell line are indicated at the top.

## KEY RESOURCES TABLE

| REAGENT or RESOURCE | SOURCE | IDENTIFIER |
|---|---|---|
| Antibodies | | |
| Anti-sAC | CEP Biotech Inc. | R21 |
| HA-Tag | Cell Signaling Technology | C29F4; Cat#3724; RRID: AB_1549585 |
| YAP | Cell Signaling Technology | D8H1X; Cat#14074; RRID:AB_2650491 |
| Phospho-Ser397 YAP | Cell Signaling Technology | D1E7Y; Cat#13619; RRID:AB_2650554 |
| Phospho-Ser127 YAP | Cell Signaling Technology | D9W2I; Cat#13008; RRID:AB_2650553 |
| Phospho-Ser109 YAP | Cell Signaling Technology | Cat#46931; RRID:AB_2799315 |
| Lats1 | Cell Signaling Technology | C66B5; Cat#3477; RRID:AB_2133513 |
| Lats1 | Cell Signaling Technology | Cat#9153; RRID:AB_2296754 |
| Phospho-Thr1079 Lats1 | Cell Signaling Technology | D57D3; Cat#8654; RRID:AB_10971635 |
| Phospho-Ser909 Lats1 | Cell Signaling Technology | Cat#9157; RRID:AB_2133515 |
| TAZ | Cell Signaling Technology | D3I6D; Cat#70148; RRID:AB_2799776 |
| Phospho-Ser89 TAZ | Cell Signaling Technology | E1X9C; Cat#59971; RRID:AB_2799578 |
| GAPDH | Cell Signaling Technology | 14C10; Cat#2118; RRID:AB_561053 |
| Beta-tubulin | Sigma | TUB2.1; Cat#T4026; RRID:AB_477577 |
| Histone H3 | Abcam | Cat#ab1791; RRID:AB_302613 |
| Cytochrome C | Santa Cruz | 2CYTC-199; Cat#sc-81752; RRID:AB_1122048 |
| Donkey anti-mouse A647 | ThermoFisher Scientific | Cat#A-31571; RRID:AB_162542 |
| Donkey anti-rabbit A488 | ThermoFisher Scientific | Cat#A-21206; RRID:AB_2535792 |
| Donkey anti-rabbit A647 | ThermoFisher Scientific | Cat#A-31573; RRID:AB_2536183 |
| HRP linked anti-rabbit IgG | Cell Signaling Technology | Cat#7074; RRID:AB_2099233 |
| HRP linked anti-mouse IgG | Cytiva | Cat#NXA931; RRID:AB_772209 |
| Ki67 | Cell Signaling Technology | Cat#12202; RRID:AB_2620142 |
| Bacterial and virus strains | | |
| Lentiviral-based non-targeting shRNA control | Origene | Cat#TR30021V |
| Lentiviral based LATS1 knock-down | Dharmacon | Cat#RMM4532-E-EG50523 |
| Lentiviral based LATS2 knock-down | Dharmacon | Cat#RMM4532-EG16798 |
| Lentiviral based YAP knock-down (pRRL.SFFV.GFP.mirE.PGK.Neo.Yap1.891) | Laboratory of Lukas Edward Dow | N/A |
| Lentiviral based TAZ knock-down (pRRL.SFFV.GFP.mirE.PGK.Neo.Wwtr1.1533) | Laboratory of Lukas Edward Dow | N/A |
| DH10B Competent *E. coli* cells | ThermoFisher Scientific | Cat#EC0113 |
| Biological samples | | |
| Primary cutaneous malignant melanomas tissue blocks (see Table S1 in supplemental information for further details) | Department of Pathology at the Mount Sinai Hospital | N/A |

| REAGENT or RESOURCE | SOURCE | IDENTIFIER |
|---|---|---|
| Chemicals, peptides, and recombinant proteins | | |
| Doxycycline hyclate | Sigma | Cat#D9891 |
| IBMX (3-Isobutyl-1-methylxanthine | Sigma | Cat#I7018 |
| PGE2 (Prostaglandin E2) | Tocris | Cat#2296 |
| Isoproterenol hydrochloride | Calbiochem | Cat#420355 |
| LRE1 | Sigma | Cat# SML1857 |
| KT5720 | Sigma | Cat#K3761 |
| TRULI | Tri-I TDI; Kastan et al., 2021 | N/A |
| Leptomycin B | Cayman Chemical Company | Cat# 10004976 |
| Cycloheximide | Sigma | Cat# 01810 |
| Critical commercial assays | | |
| cAMP complete ELISA kit | ENZO Life Sciences | Cat#ADI-901-066 |
| Nuclei Isolation Kit: Nuclei EZ Prep | Sigma | Cat#NUC101-1KT |
| CellTiter-Glo® 2.0 assay | Promega | Cat#G9242 |
| Deposited data | | |
| RNA-seq on cells expressing cAMP microdomains | This paper | GEO; GSE154877 |
| RNA-seq on tumors expressing cAMP microdomains | This paper | GEO; GSE154877 |
| ATAC-seq on cells expressing nuclear cAMP microdomain | This paper | GEO; GSE154877 |
| Experimental models: Cell lines | | |
| *Adcy10*$^{-/-}$ and *Adcy10*$^{WT/WT}$ melanocytes | Zippin Laboratory | Zhou et al., 2018 |
| Mel 2-4 line (sAC$^{KO}$) | This paper; Zippin Laboratory | N/A |
| Mel 2-4 NLS-sAC | This paper; Zippin Laboratory | N/A |
| Mel 2-4 NES-sAC | This paper; Zippin Laboratory | N/A |
| Mel 2-4 Mito sAC | This paper; Zippin Laboratory | N/A |
| SK-Mel 2 | Taha Merghoub | N/A |
| SK-Mel 90 | Taha Merghoub | N/A |
| SK-Mel 178 | Taha Merghoub | N/A |
| SK-Mel 266 | Taha Merghoub | N/A |
| Yummer1.7 | Taha Merghoub | N/A |
| SCC12 | Laboratory of Loraine Gudas | N/A |
| DLD1 | Laboratory of Lukas Edward Dow | N/A |
| SW480 | Laboratory of Lukas Edward Dow | N/A |
| Hs766t | Laboratory of Lewis Cantley | N/A |
| PANC1 | Laboratory of Lewis Cantley | N/A |
| MIAPaCa2 | Laboratory of Lewis Cantley | N/A |
| LNCaP | Laboratory of Christopher Barbieri | N/A |
| M263 | Laboratory of Roger Lo | N/A |
| Experimental models: Organisms/strains | | |
| NSG mice | Weill Cornell Medical College | N/A |

| REAGENT or RESOURCE | SOURCE | IDENTIFIER |
|---|---|---|
| Oligonucleotides | | |
| List of primers used for cloning (see Table S2 in supplemental information) | N/A | N/A |
| List of primers used for RT-PCR analyses (see Table S3 in supplemental information) | N/A | N/A |
| Recombinant DNA | | |
| pCW57.1 | N/A | Addgene plasmid Cat#41393 |
| pcDNA3-ICUE3 | DiPilato and Zhang, 2009 | Addgene plasmid Cat#61622 |
| GFP-PKI nls | Billiard et al., 2001 | Addgene plasmid |
| pLL3.7-EF-EYFP-YAP1_WT-PolyA | Ege et al., 2018 | Addgene plasmid Cat#112284 |
| pQCXIH-Myc-YAP | Zhao et al., 2007 | Addgene plasmid Cat#33091 |
| pQCXIH-Myc-YAP-5SA | Zhao et al., 2007 | Addgene plasmid Cat#33093 |
| pQCXIH-Flag-YAP-S127A | Zhao et al., 2007 | Addgene plasmid Cat#33092 |
| pQCXIH-Flag-YAP-S381A | Zhao et al., 2010 | Addgene plasmid Cat#33068 |
| EYFP-YAP-S397A | This paper | N/A |
| Software and algorithms | | |
| ImageJ 2.0 | Schneider et al., 2012 | https://imagej.nih.gov/ij/ |
| GraphPad Prism 8.0 | GraphPad Software | N/A |
| Image Lab 6.1 | Bio-Rad Laboratories | N/A |
| Other | | |
| Doxycycline chow (Global 2018 base with 625 mg/kg doxycycline hyclate) | Teklad | Cat#TD.01306 |
| Matrigel Basement Membrane Matrix | Corning | Cat#354248 |
| Matrigel matrix solution | Corning | Cat#356231 |